JAMES | Journal of Advances in Modeling Earth Systems

RESEARCH ARTICLE
10.1029/2020MS002333

Special Section:
Dynamical cores of oceanic models across all scales and their evaluation

The Geography of Numerical Mixing in a Suite of Global Ocean Models

R. M. Holmes[1,2], J. D. Zika[2], S. M. Griffies[3], A. McC. Hogg[4], A. E. Kiss[4], and M. H. England[1]

[1]Climate Change Research Centre and ARC Centre of Excellence for Climate Extremes, University of New South Wales, Sydney, NSW, Australia, [2]School of Mathematics and Statistics, University of New South Wales, Sydney, NSW, Australia, [3]NOAA Geophysical Fluid Dynamics Laboratory & Princeton University Program in Atmospheric and Oceanic Sciences, Princeton, NJ, USA, [4]Research School of Earth Sciences and ARC Centre of Excellence for Climate Extremes, Australian National University, Canberra, NSW, Australia

Key Points:

- A tracer budget residual method is presented for estimating the spatial structure of numerical mixing in global ocean models
- Numerical mixing of temperature can drive diathermal heat transport of similar magnitude to parameterized physical mixing
- Numerical mixing of temperature is prominent in the tropical thermocline and eddy active boundary current regions

Correspondence to:
R. M. Holmes,
ryan.holmes@unsw.edu.au

Citation:
Holmes, R. M., Zika, J. D., Griffies, S. M., Hogg, A. M., Kiss, A. E., & England, M. H. (2021). The geography of numerical mixing in a suite of global ocean models. *Journal of Advances in Modeling Earth Systems*, *13*, e2020MS002333. https://doi.org/10.1029/2020MS002333

Received 28 SEP 2020
Accepted 2 JUN 2021

Abstract Numerical mixing, defined here as the physically spurious tracer diffusion due to the numerical discretization of advection, is known to contribute to biases in ocean models. However, quantifying numerical mixing is nontrivial, with most studies utilizing targeted experiments in idealized settings. Here, we present a water mass transformation-based method for quantifying numerical mixing that can be applied to any conserved variable in general circulation models. Furthermore, the method can be applied within individual fluid columns to provide spatial information. We apply the method to a suite of global ocean model simulations with differing grid spacings and subgrid-scale parameterizations. In all configurations numerical mixing drives diathermal heat transport of comparable magnitude to that associated with explicit parameterizations. Numerical mixing is prominent in the tropical thermocline, where it is sensitive to the vertical diffusivity and resolution. At colder temperatures numerical mixing is sensitive to the presence of explicit neutral diffusion, suggesting that it may act as a proxy for neutral diffusion when it is explicitly absent. Comparison of otherwise equivalent 1/4° and 1/10° configurations with grid-scale dependent horizontal viscosity shows only a modest enhancement in numerical mixing at 1/4°. However, if the lateral viscosity is maintained while resolution is increased then numerical mixing is reduced by almost 35%. This result suggests that the common practice of reducing viscosity in order to maximize permitted variability must be considered carefully. Our results provide a detailed view of numerical mixing in ocean models and pave the way for improvements in parameter choices and numerical methods.

Plain Language Summary Numerical ocean circulation models are useful tools for studying the ocean's role in climate and providing projections of climate change. However, due to constraints on computational power, numerical models must represent processes that are continuous in the real ocean using discrete approximations. One consequence of such discrete approximations is numerical mixing, whereby seawater transport (a process that should not mix properties such as heat and salt content) results in mixing and exchange of properties with surrounding seawater. Mixing in the ocean interior is weak, and so the presence of additional numerical mixing in ocean models can cause the models to drift away from reality, reducing their accuracy and utility. In this study, we present a new method for quantifying numerical mixing in global ocean models, including its three-dimensional spatial structure. Most previous quantifications of numerical mixing have been performed in idealized model configurations or have provided only bulk ocean basin-integrated estimates. We apply our method to temperature within a suite of global ocean circulation models with differing grid resolutions and model parameters. Our results will help modelers understand the consequences and trade-offs involved in choosing model parameters in order to maximize model accuracy and utility.

1. Introduction

Numerical ocean general circulation models are useful tools for studying ocean dynamics, interpreting observations and providing predictions of past and future circulation states (Griffies et al., 2009; Fox-Kemper et al., 2019). However, numerical models are necessarily approximate in that they represent continuous physical processes using discrete operators. These discrete representations can impact the accuracy

of model integrations. For example, numerical issues have been invoked to explain eastern boundary upwelling region biases in climate models (Richter, 2015), inaccurate representation of deep water circulation (Lee et al., 2002), problems with sea ice formation (Naughten et al., 2017), and the spurious uptake of heat (Adcroft et al., 2019).

1.1. The Numerical Mixing Problem

In this article, we focus on tracer mixing associated with the numerical representation of advection. This mixing leads to the spurious diffusion or anti-diffusion of tracer gradients. From a simple perspective, numerical mixing arises because advective tracer fluxes entering a finite-sized grid cell are mixed throughout that cell. This process contrasts to the continuum whereby advection, in the absence of physical mixing sources, preserves all tracer moments.

Depending on their leading order truncation error, numerical advection schemes are classed as either diffusive (e.g., first-order upwind) or dispersive (e.g., second-order centered). Dispersive advection schemes can create tracer extrema and oscillations that are particularly problematic through coupling with physical processes such as convection (Griffies et al., 2000; Hecht, 2010; Naughten et al., 2017). To avoid creating extrema, these schemes are usually combined with flux limiters (and/or explicit diffusion) that maintain monotonicity in the tracer distribution. However, the associated numerical diffusion can often exceed the diffusion expected in the physical system, particularly in the ocean interior where physical sources of diapycnal diffusion are weak such that water-mass properties are retained over long time periods (e.g., Ledwell et al., 2011). Furthermore, numerical diffusion is not constrained by the same laws as those that govern physical diffusion. While numerical advection schemes are increasing in sophistication and accuracy, spurious numerical diffusion is still a leading issue thought to affect processes such as ocean heat uptake, transport and model drift (Adcroft et al., 2019; Griffies et al., 2015; Hill et al., 2012; Holmes et al., 2019; Holmes et al., 2019a; Ilicak et al., 2012; Lee et al., 2002; Megann, 2017).

As global ocean models move toward mesoscale eddy-permitting and eddy-resolving resolutions, the importance of numerical closure schemes increases. Poorly resolved yet energetic flows near the grid-scale generally lead to enhanced spurious mixing (Griffies et al., 2000; Ilicak et al., 2012). Yet further increases in resolution, if accompanied by decreases in explicit diffusion and viscosity parameters through grid-scale or flow-aware scalings, may not necessarily be expected to reduce spurious mixing due to the net down-scale (toward smaller scale) cascade of enstrophy and tracer variance active in geostrophic turbulence (Roberts & Marshall, 1998; Soufflet et al., 2016). Recent studies have highlighted the particular importance of lateral viscosity and momentum closure for controlling spurious mixing by arresting this cascade at scales somewhat larger than the grid-scale (Ilicak, 2016; Ilicak et al., 2012). That is, numerical spurious mixing would be made negligible if grid-scale tracer and velocity gradients were small enough. Numerical convergence could be achieved by refining resolution while keeping explicit diffusion and viscosity parameters constant or by increasing explicit diffusion and viscosity (e.g., Griffies et al., 2000; Griffies & Treguier, 2013; Ilicak, 2016; Ilicak et al., 2012; Lévy et al., 2010). However, such concerns have yet to be fully incorporated into global general circulation models where parameters are often chosen to enhance eddy energy and boundary current strength; for practical (computational cost) reasons; or for numerical stability-based reasons.

1.2. Measuring Numerical Mixing

Some of the uncertainty around parameters and numerical schemes in ocean models stem from the difficulty in accurately quantifying numerical mixing and measuring where such mixing is prevalent. In the case of relatively simple, low-order and linear advection schemes without flux limiters, the source of spurious mixing due to numerical truncation can be analytically isolated (e.g., Maqueda & Holloway, 2006; Marchesiello et al., 2009; Soufflet et al., 2016). For nonlinear and/or high-order schemes with limiters, analytical results are generally unavailable. Hence, numerical experiments are generally needed to compare advection schemes and to quantify the numerical mixing arising from any particular process (e.g., Burchard & Rennau, 2008; Getzlaff et al., 2010; Hill et al., 2012; Klingbeil et al., 2014).

Indirect methods of evaluating spurious mixing are often based on ideas from water-mass transformation (Groeskamp et al., 2019) or energetic ideas (Ilicak et al., 2012), where numerical mixing is inferred from

changes in the distribution of volume or mass in tracer or density coordinates, or by changes in the background potential energy. However, many of these methods yield either a single global measure (e.g., Gibson et al., 2017; Ilicak et al., 2012) or basin-scale averages of numerical mixing whose relation to local processes is unclear (e.g., Griffies et al., 2000; Lee et al., 2002; Megann, 2017; Urakawa & Hasumi, 2014). These methods do not resolve the spatial structure of numerical mixing and therefore render a detailed examination of its causes rather difficult or unavailable. Furthermore, many of these methods rely on estimating changes in tracer-coordinate distributions in idealized configurations where advection is the sole transport process, so that any other process that may influence the tracer distribution, such as surface forcing and parameterizations of subgrid-scale physical processes, are artificially turned off (e.g., Griffies et al., 2000; Ilicak, 2016; Ilicak et al., 2012; Riemenschneider & Legg, 2007). Alternatively, the relative role of numerical and physical mixing must be estimated using parameter dependence and/or scaling arguments (e.g., Lee et al., 2002; Megann, 2017; Roberts & Marshall, 1998).

1.3. New Approach Taken Here

In this article, we introduce a new method to quantify the temporal and three-dimensional spatial structure of numerical tracer mixing in realistic, global ocean models. Our method, here applied to temperature, is based on ideas from water-mass transformation. We construct a budget for what has been called the 'internal heat content' (Holmes et al., 2019a, hereafter HZE19) of temperature layers within each vertical grid column. The transport of heat across isotherms due to numerical mixing can be calculated as the residual of this budget. The internal heat content provides an integrated form of the heat content which removes much of the rapid variability in the heat content of temperature layers due to adiabatic and diabatic volume exchanges. Its use for measuring spurious mixing reduces the sensitivity of our results to noise in contrast to previous approaches based on volume transports (e.g., Lee et al., 2002; Megann, 2017; Urakawa & Hasumi, 2014). Our calculations are also performed online to avoid errors associated with temporal averaging or sub-sampling.

The diagnostic method used here could be applied to any conserved tracer field (e.g., temperature, salinity or passive tracers such as CFCs). We chose to focus on temperature given its direct connection to climate and sea level. Although our method is unable to separate the diapycnal and isopycnal components of numerical diffusion, it provides a robust and detailed picture of the impact of numerical diffusion on the simulated heat budget. The numerical and physical picture arising from this analysis offers the first compelling view of the geography of numerical mixing in realistic global simulations, with this view providing direct guidance for modelers aiming to ameliorate such mixing.

1.4. Content of This Paper

The new diagnostic method is described in Section 2 and applied to a suite of global ocean sea-ice models described in Section 3. In contrast to studies performed in idealized contexts, which are often focused on the sensitivity to different numerical tracer and momentum advection schemes, here we make use of standard numerical schemes employed as part of realistic global simulations. Although here implemented in the widely used MOM5 code (Modular Ocean Model, version 5; Griffies, 2012), our method could equally be applied to other ocean model codes.

As we show in this study, numerical mixing drives across-isotherm heat fluxes of comparable magnitude to those associated with explicitly parameterized mixing in all model configurations examined here. Numerical mixing is prominent in eddying regions such as the Western Boundary Currents (WBCs) and the Antarctic Circumpolar Current (ACC) as well as the tropical thermocline (Section 4). In regions of active mesoscale eddies, numerical mixing is sensitive to the presence of explicit mesoscale mixing parameterizations, particularly neutral diffusion (Section 5.1). Numerical mixing in the tropics at warm temperatures is instead sensitive to the background vertical diffusivity and the vertical grid spacing (Sections 5.2 and 5.3). Numerical mixing is most prominent at eddy-permitting resolution (1/4°), reduced at finer resolution (1/10°) and most reduced at coarse (1°) resolution (Section 5.5). However, much of this variation in numerical mixing with resolution is due to differences in explicit mixing parameters. Our results are summarized and some perspectives given in Section 6. Appendix A provides details concerning the implementation of our

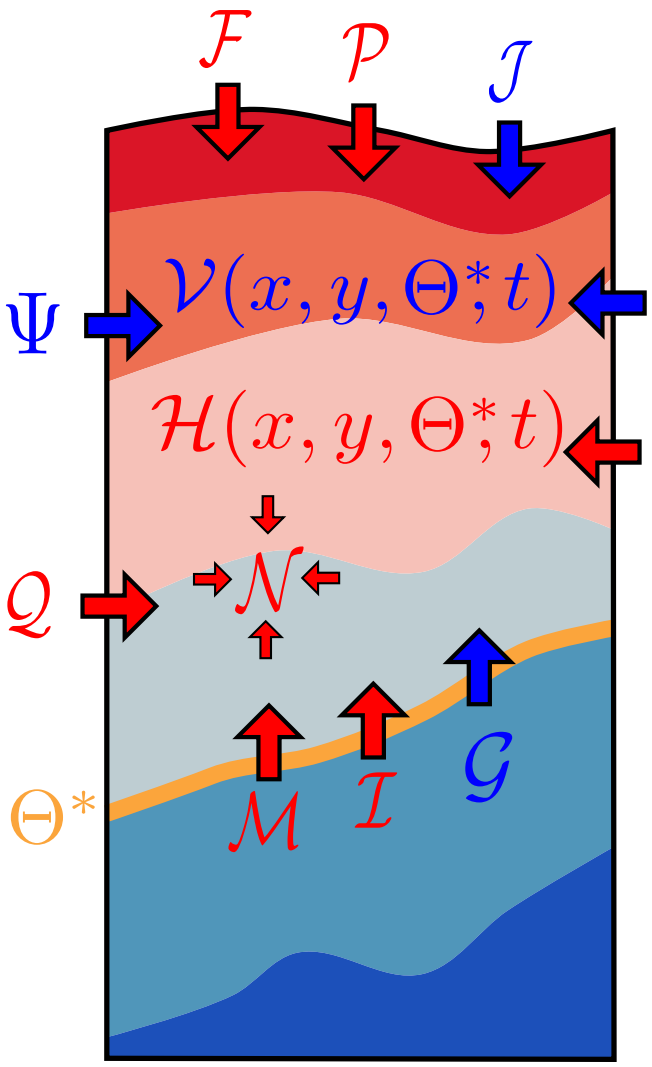

Figure 1. A fluid column for which budgets are constructed for the volume, $\mathcal{V}(x,y,\Theta^*,t)$ and heat content, $\mathcal{H}(x,y,\Theta^*,t)$, per unit horizontal area of water warmer than a given temperature Θ^* (orange isotherm) (Equations 2 and 4). Red (blue) colors indicate warmer (colder) water. Each term in the budget corresponds to the convergence of the associated fluxes into the region of interest divided by the horizontal area of the fluid column, meaning that heat and volume budget terms have the units of W m^{-2} and m s^{-1} respectively. Note that we do not require the temperature stratification to be stable, although the column is drawn as such. The volume budget includes terms (blue arrows) associated with surface volume fluxes $\mathcal{J}$, lateral volume transport Ψ and volume transport $\mathcal{G}$ across the Θ^* isotherm. The heat budget includes terms (red arrows) associated with lateral heat transport $\mathcal{Q}$, surface heat fluxes $\mathcal{F}$ (where the surface heat flux associated with the surface volume fluxes $\mathcal{P}$ is treated separately), explicitly parameterized neutral diffusion $\mathcal{N}$, vertical mixing $\mathcal{M}$ and numerical mixing $\mathcal{I}$. Note that $\mathcal{F}$ includes only the solar radiation that is absorbed above the Θ^* isotherm.

diagnostic method, and Appendix B discusses the role of subgrid scale eddy advection and skew diffusion within the heat budgets.

2. Methods

Our method for quantifying numerical mixing follows from the global diathermal heat budget analysis of HZE19. Here we apply the same procedure to the heat and volume budgets of the fluid within each water column that is warmer than some temperature Θ^* (Figure 1, where Θ^* is an independent variable). For convenience, we work throughout the article with budgets divided by the horizontal area of the water column (an area which remains constant in time). The heat budget terms are therefore given in units of W m^{-2} and the volume budget terms are given in units of $m^3\ s^{-1}\ m^{-2} = m\ s^{-1}$.

2.1. The Volume Budget of Fluid Columns

The volume per unit horizontal area of fluid (units of m) within a fluid column warmer than Θ^* is given by

$$\mathcal{V}(x,y,\Theta^*,t) = \int_{\Theta(x,y,z,t)>\Theta^*} dz, \tag{1}$$

where $\Theta(x, y, z, t)$ is the temperature of the fluid column located at x, y. As defined, $\mathcal{V}(x,y,\Theta^*,t)$ is equivalent to the depth of the Θ^* isotherm if the column is stably stratified in temperature. However, as per traditional water mass analysis formulations (e.g., Groeskamp et al., 2019), we do not require that the fluid column be stably stratified in temperature. $\mathcal{V}$ obeys the budget equation (see blue arrows in Figure 1)

$$\frac{\partial \mathcal{V}}{\partial t}(x,y,\Theta^*,t) = \mathcal{G} + \mathcal{J} + \Psi, \tag{2}$$

where $\mathcal{J}$ is the surface volume flux (per unit horizontal area) into the fluid column where the surface temperature is greater than Θ^*; Ψ measures the transport of volume into the column from adjacent fluid columns above the Θ^* isotherm; and $\mathcal{G}$ measures the volume transport, or water-mass transformation, across the Θ^* isotherm associated with the various diabatic processes (including numerical mixing), where the associated flux convergences are once again divided by the horizontal area of the water column.

2.2. The Heat Budget of Fluid Columns

The heat content (per unit horizontal area in units of J m^{-2}) of the fluid warmer than Θ^* within each column is

$$\mathcal{H}(x,y,\Theta^*,t) = \rho_0 C_p \int_{\Theta(x,y,z,t)>\Theta^*} \Theta(x,y,z,t) dz, \tag{3}$$

where in our simulations ρ_0 is a constant reference density corresponding to the Boussinesq approximation and C_p is a constant specific heat capacity (our simulations use Conservative Temperature as the prognostic temperature variable, McDougall, 2003; McDougall & Barker, 2011). $\mathcal{H}$ obeys the budget equation (see Figure 1)

$$\frac{\partial \mathcal{H}}{\partial t}(x,y,\Theta^*,t) = \mathcal{M} + \mathcal{N} + \mathcal{F} + \mathcal{P} + \mathcal{Q} + \rho_0 C_p \Theta^* \mathcal{G} + \mathcal{I}, \tag{4}$$

where $\mathcal{M}$ is the diffusive heat transport across the Θ^* isotherm due to vertical mixing, $\mathcal{N}$ accounts for explicitly parameterized neutral diffusion, $\mathcal{I}$ accounts for numerical mixing, $\mathcal{F}$ accounts for surface heat fluxes where the component associated with surface volume fluxes, $\mathcal{P}$, is treated separately, $\mathcal{Q}$ captures the lateral heat transport into the column from adjacent fluid columns above the Θ^* isotherm (not including the portion associated with neutral diffusion in $\mathcal{N}$) and the term involving $\mathcal{G}$ is the across-isotherm heat transport associated with across-isotherm volume transport. As for the volume budget, each term in Equation 4 corresponds to a flux convergence of the given process within the volume $\mathcal{V}$ divided by the horizontal area of the fluid column, so that each term has units of W m^{-2}.

If a process contributes a positive tendency to the heat budget in Equation 4, then that process contributes to an increase in heat content for the ocean region with temperature $\Theta > \Theta^*$. In particular, down-gradient diffusive mixing decreases the heat content in the $\Theta > \Theta^*$ region as it mixes warm waters with cooler waters; i.e., the water in the $\Theta > \Theta^*$ region becomes cooler via down-gradient diffusive mixing.

2.3. The Internal Heat Budget of Fluid Columns

It is difficult to use the full heat budget, Equation 4, to estimate numerical mixing because of the across-isotherm volume transport term $\mathcal{G}$. Across-isotherm volume fluxes occur because of a convergence of the non-advective heat fluxes within temperature intervals leading to heating or cooling of the fluid within the given interval (Walin, 1982, see Equation 14 of HZE19). The full heat budget therefore effectively includes effects of each non-advective heat flux twice; once through its diffusive flux (e.g., $\mathcal{M}$ in Equation 4) and once through the across-isotherm heat transport associated with its induced across-isotherm volume transport (e.g., the contribution of $\mathcal{M}$ to $\mathcal{G}$ in Equation 4). The second contribution through the across-isotherm volume flux can be noisy because it depends on the *convergence* (in temperature space) of the nonadvective fluxes (e.g., $\partial\mathcal{M}/\partial\Theta^*$). Furthermore, the contribution of across-isotherm volume fluxes to the heat budget is arbitrary in an absolute sense because it depends on the reference temperature or temperature units (being multiplied by Θ^* in Equation 4).

Following HZE19, we formulate a budget for the *internal* heat content, with this budget independent of $\mathcal{G}$. The internal heat is defined as

$$\mathcal{H}_I(x,y,\Theta^*,t) \equiv \mathcal{H} - \rho_0 C_p \Theta^* \mathcal{V} = \rho_0 C_p \int_{\Theta^*}^{\infty} \mathcal{V} \mathrm{d}\Theta. \tag{5}$$

Substitution of $\mathcal{G}$ from the volume budget Equation 2 into Equation 4 leads to a budget for internal heat

$$\frac{\partial \mathcal{H}_I}{\partial t}(x,y,\Theta^*,t) = \mathcal{M} + \mathcal{N} + \mathcal{F} + \mathcal{P}_I + \mathcal{Q}_I + \mathcal{I}, \tag{6}$$

where

$$\mathcal{P}_I = \mathcal{P} - \rho_0 C_p \Theta^* \mathcal{J}, \tag{7}$$

$$\mathcal{Q}_I = \mathcal{Q} - \rho_0 C_p \Theta^* \Psi, \tag{8}$$

are "internal" equivalents of the surface and lateral heat transport terms, respectively. Again, each term in Equation 6 has units of W m^{-2}.

As a consequence of the integration in Equation 5, the internal heat content and its budget (Equation 6) are smoother and less affected by noise than the full heat content $\mathcal{H}$ (see HZE19, in particular their Figure A1). The internal heat content budget effectively corresponds to the integral of the volume budget multiplied by $\rho_0 C_p$, and it does not contain the problematic water-mass transformation volume transport $\mathcal{G}$. Every term in Equation 6 can be calculated at every horizontal grid cell for any given isotherm temperature Θ^* except the heat transport across the Θ^* isotherm due to numerical mixing, $\mathcal{I}(x,y,\Theta^*,t)$. Hence, we infer $\mathcal{I}$ by com-

puting the residual of the other terms in the internal heat budget. The calculation provides an estimate of the transport of heat across isotherms associated with numerical mixing as a function of temperature, and time, within each fluid column. More details of how the calculation is implemented numerically are given in Appendix A, as well as a discussion of the known limitations and their implications.

The area-integral of $\mathcal{I}(x,y,\Theta^*,t)$ is the global diathermal heat transport due to numerical mixing discussed by HZE19,

$$\mathcal{I}^g(\Theta^*,t) \equiv \iint \mathcal{I}(x,y,\Theta^*,t)\mathrm{d}x\mathrm{d}y = \frac{\partial \mathcal{H}_I^g}{\partial t} - \mathcal{F}^g - \mathcal{P}_I^g - \mathcal{N}^g - \mathcal{M}^g, \tag{9}$$

where the relevant area element $\mathrm{d}x\,\mathrm{d}y$ is horizontal, and where $\mathcal{I}^g$ has units of Watts. In the second equality we have written $\mathcal{I}^g$ as a residual of Equation 6, where the superscript g indicates the global area-integral under which $\mathcal{Q}_I$ drops out. $\mathcal{I}^g$ will be compared across our model suite in Section 5.

2.4. Relation to Heat Variance Dissipation Rate

Negative values of $\mathcal{I}$ contribute to a decrease in heat content for the ocean region with $\Theta > \Theta^*$. We expect such contributions if the numerical mixing fluxes temperature down-gradient; i.e., from warm to cold. We also expect this contribution for an advection scheme that is monotonic, since flux limiters generally add mixing in regions where extrema would otherwise arise. Such down-gradient mixing, in turn, leads to the dissipation of temperature variance.

A connection to diffusive mixing can be made precise by defining a diffusive heat flux, $\mathbf{B}(\mathbf{x}, t)$, associated with the numerical mixing via

$$\mathcal{I}^g(\Theta^*,t) \equiv \iint_{\Theta=\Theta^*} \mathbf{B}\cdot\hat{\mathbf{n}}\mathrm{d}\mathcal{S} = \iint_{\Theta=\Theta^*} \mathbf{B}\cdot\nabla\Theta\,\frac{\mathrm{d}\mathcal{S}}{|\nabla\Theta|}. \tag{10}$$

In this equation, $\hat{\mathbf{n}} = \nabla\Theta / |\nabla\Theta|$ is the normal vector pointing up the temperature gradient (toward warmer water), and $\mathrm{d}\mathcal{S}$ is the area-element on the Θ^* isotherm. Using the fundamental theorem of calculus as detailed in Marshall et al. (1999) and Groeskamp et al. (2019), the area-integral in Equation 10 can be converted to a volume integral,

$$\mathcal{I}^g(\Theta^*,t) = -\frac{\partial}{\partial\Theta^*}\iiint_{\Theta>\Theta^*} \mathbf{B}\cdot\nabla\Theta\mathrm{d}V, \tag{11}$$

with the minus sign arising from our choice to focus on waters that are warmer than Θ^*. Now express $\mathbf{B}$ in terms of a rank-2 numerical diffusivity tensor, $\mathbb{K}_{\mathrm{num}}(\mathbf{x},t)$, so that

$$\mathbf{B}(\mathbf{x},t) = -\rho_0 C_p \mathbb{K}_{\mathrm{num}}\cdot\nabla\Theta, \tag{12}$$

then Equation 11 becomes

$$\mathcal{I}^g(\Theta^*,t) = \frac{\partial}{\partial\Theta^*}\iiint_{\Theta>\Theta^*} \frac{1}{2} D_{\mathrm{num}}\mathrm{d}V. \tag{13}$$

The integrand of Equation 13 is half the rate of dissipation of temperature "variance", $\rho_0\, C_p\, \Theta^2$, achieved by numerical mixing as derived by Burchard and Rennau (2008),

$$D_{\mathrm{num}} \equiv 2\rho_0 C_p \nabla\Theta\cdot\mathbb{K}_{\mathrm{num}}\cdot\nabla\Theta. \tag{14}$$

Only the symmetric component of $\mathbb{K}_{\mathrm{num}}$ influences the temperature variance with D_{num} a symmetric quadratic form (e.g., see chapter 13 of Griffies, 2004).

For physical diffusion, the diffusivity tensor is positive so that the tracer dissipation is negative, $D_{\text{physics}} \equiv 2\rho_0 C_p \nabla\Theta \cdot \mathbb{K}_{\text{physics}} \cdot \nabla\Theta < 0$, which follows since physical diffusion fluxes are strictly down-gradient. However, for numerically induced mixing there is no guarantee that temperature variance will be dissipated; i.e., the numerical diffusivity tensor, $\mathbb{K}_{\text{num}}$, need not be positive. For example, a non-monotonic advection scheme can increase temperature variance by driving an up-gradient temperature flux. Burchard and Rennau (2008) estimate D_{num} directly in three-dimensional Eulerian space by comparing the advected square of a tracer to the square of the advected tracer. Our metric $\mathcal{I}^g$ (and its spatially resolved field $\mathcal{I}$) instead corresponds to a volume integral of the temperature variance dissipation rate over all fluid within a given temperature band (Equation 13).

2.5. Relation to Effective Diffusivity

$\mathcal{I}^g$ can also be related to the concept of an effective diffusivity used by Griffies et al. (2000) to quantify spurious mixing in an idealized setting. The effective diffusivity acting on temperature is defined by the vertical diffusivity κ_{eff} that would yield the same diathermal heat transport $\mathcal{I}^g$ if the ocean's temperature field was re-sorted such that isotherms were flat. That is

$$\kappa_{\text{eff}}(\tilde{z}) = -\left(\rho_0 C_p A(\tilde{z}) \frac{\partial\tilde{\Theta}}{\partial\tilde{z}}\right)^{-1} \mathcal{I}^g(\tilde{\Theta}(\tilde{z})), \tag{15}$$

where $\tilde{\Theta}(\tilde{z})$ is the re-sorted temperature at the depth $\tilde{z}$ and $A(\tilde{z})$ is the area of the ocean at depth $\tilde{z}$. κ_{eff} is proportional to $\mathcal{I}^g$ through a factor dependent on the ocean's area and temperature distribution ($\tilde{\Theta}(\tilde{z})$ can be easily related to $\mathcal{V}(\Theta^*)$ and $A(\tilde{z})$). However, not only is re-sorting of the temperature field problematic in a realistic global ocean model with disconnected basins, but the κ_{eff} so derived is a large-scale average that is not easily related to the small-scale point-wise diffusivity associated with numerical mixing that is often restricted to only small regions. The background potential energy metric of Ilicak et al. (2012); Gibson et al. (2017), or the local method of Ilicak (2016), suffer from similar issues when applied outside of an idealized setting. For these reasons, $\mathcal{I}^g$ is a more suitable objective metric appropriate for a realistic global model.

2.6. A Global Summary Metric

Integrating $\mathcal{I}^g$ across all temperatures yields a summary metric for the total amount of numerical mixing within a given simulation,

$$\mathcal{I}_{\text{net}}(t) \equiv -\int_{-\infty}^{\infty} \mathcal{I}^g(\Theta^*, t)\mathrm{d}\Theta^*, \tag{16}$$

with $\mathcal{I}_{\text{net}}$ measured here in units of PW °C. From Equation 11, $\mathcal{I}_{\text{net}}$ also corresponds to the global volume integrated heat variance dissipation rate,

$$\mathcal{I}_{\text{net}}(t) = -\iiint \mathbf{B} \cdot \nabla\Theta \, \mathrm{d}V. \tag{17}$$

Therefore, when globally integrated, our technique based on temperature binning should yield equivalent results to the Eulerian approach of Burchard and Rennau (2008).

3. Models

We analyze a suite of global ocean sea-ice model simulations performed using the ACCESS-OM2 modeling framework (Kiss et al., 2020), which couples together the Modular Ocean Model version 5.1 (MOM5, Griffies, 2012) and the Los Alamos Sea Ice Model version 5.1.2 (CICE, Hunke et al., 2015). ACCESS-OM2 configurations are available at 1° (ACCESS-OM2-1), 1/4° (ACCESS-OM2-025) and 1/10° (ACCESS-OM2-01) horizontal resolution. Forcing is taken from the JRA55-do reanalysis (Tsujino et al., 2018) and consists

Table 1
A Summary of the Various Model Configurations

Configuration	Horizontal spacing	Vertical levels	Background κ ($m^2 s^{-1}$)	Neutral physics	Spin-up (analysis) years	$\mathcal{I}_{net}$ (PW°C)
025	1/4°	KDS50	0	none	162 (10)	19.6
025-N	1/4°	KDS50	0	ND	162 (10)	15.8
025-NG	1/4°	KDS50	0	ND + GM	162 (10)	14.9
025-NG-kb5	1/4°	KDS50	10^{-5}	ND + GM	164 (10)	10.8
025-NG-kbv	1/4°	KDS50	5×10^{-6} (J09)	ND + GM	164 (10)	13.0
025-KDS75	1/4°	KDS75	10^{-6}	none	162 (10)	16.3
1-KDS50	1°	KDS50	5×10^{-6} (J09)	ND + GM	320 (10)	7.8
1-GFDL50	1°	GFDL50	5×10^{-6} (J09)	ND + GM	320 (10)	7.5
1-KDS75	1°	KDS75	5×10^{-6} (J09)	ND + GM	320 (10)	6.3
1-KDS100	1°	KDS100	5×10^{-6} (J09)	ND + GM	320 (10)	5.5
1-KDS135	1°	KDS135	5×10^{-6} (J09)	ND + GM	320 (10)	4.9
01	1/10°	KDS75	10^{-6}	none	162 (2)	14.7
01-hvisc	1/10°	KDS75	10^{-6}	none	5 (2)	10.7

Note. KDS refers to vertical level positions chosen according to Stewart et al. (2017) while GFDL50 indicates the GFDL CM2.5 vertical levels scheme (Delworth et al, 2012). κ indicates the background vertical tracer diffusivity, with J09 indicating a reduction to 10^{-6} m^2 s^{-1} within the equatorial band (Jochum, 2009). GM refers to the eddy-transport scheme of Gent and McWilliams (1990) and ND refers to explicit neutral diffusion. Each configuration is initialized from the World Ocean Atlas 2013 version 2 (WOA13) and spun-up for the time period shown in the second last column (except for ACCESS-OM2-01-hvisc which was initialized from ACCESS-OM2-01 and run for only five years). The last column lists the globally integrated heat variance dissipation rate due to numerical mixing metric $\mathcal{I}_{net}$ discussed in Section 2.6.

of a repeating cycle of the period May 1990–April 1991 (Stewart et al., 2019). We use 13 different model configurations (see Table 1) to test sensitivity to horizontal and vertical resolution, the vertical diffusivity, neutral physics parameterizations and lateral viscosity. More information on ACCESS-OM2 is contained in Kiss et al. (2020). Below we note details particularly relevant to the current study. For more details on the numerical algorithms, the reader is referred to Griffies (2012) and the references contained therein.

MOM5 is discretized on an Arakawa B-grid. All configurations utilize the multi-dimensional piece-wise parabolic tracer method (MDPPM, Colella & Woodward, 1984) for both horizontal and vertical tracer advection with a monotonicity-preserving flux limiter following Suresh and Huynh (1997) and staggered second-order forward time stepping as described in Griffies et al. (2005) and Chapter 11 of Griffies (2012). Centered second-order schemes are used for both horizontal and vertical momentum advection with third-order Adams-Bashforth time stepping. A split explicit method is used to separate barotropic and baroclinic modes, with predictor-corrector time stepping on the barotropic mode with a time filter gamma parameter of 0.2 (see Chapter 11 of Griffies, 2012) and 160 barotropic time steps for each baroclinic time step. Horizontal friction is implemented with a biharmonic operator and a Smagorinsky scaling for the viscosity coefficient (Griffies & Hallberg, 2000). Vertical diffusion of both tracers and momentum is parameterized using a background diffusivity, the K-profile parameterization (Large et al., 1994; Van Roekel et al., 2018) and a bottom-enhanced internal tide mixing scheme (Simmons et al., 2004).

To evaluate sensitivity to the neutral physics parameterizations we compare three configurations of ACCESS-OM2-025 where the Gent-McWilliams (GM) eddy transport parameterization (Gent & McWilliams, 1990; Gent et al., 1995; Griffies, 1998) is active or inactive (with a spatial structure determined according to the "baroclinic zone" setting, see Griffies et al., 2005; Griffies, 2012), or neutral diffusion in the form of a neutral diffusivity (Griffies et al., 1998; Redi, 1982; Solomon, 1971) is active or inactive. When active, the ACCESS-OM2-025 simulations use a maximum (minimum) GM diffusivity of 200 $m^2 s^{-1}$ (1 $m^2 s^{-1}$) and a neutral diffusivity that is scaled by the grid spacing relative to the local Rossby radius with a maximum

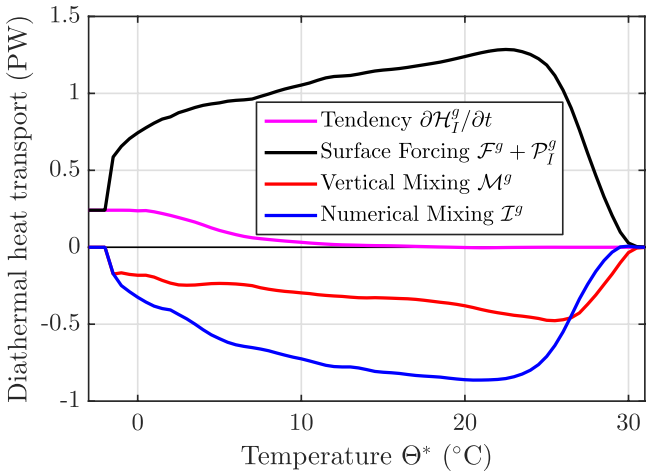

Figure 2. Globally integrated internal heat content budget (Equation 9) for ACCESS-OM2-025. Shown are the total heat transport into all water warmer than a given temperature Θ due to surface forcing $\mathcal{F}^g + \mathcal{P}_I^g$ (black); explicitly parameterized vertical mixing $\mathcal{M}^g$ (red); and numerical mixing $\mathcal{I}^g$ (blue); as well as the internal heat content tendency $\partial\mathcal{H}_I^g / \partial t$ (magenta). The global metric $\mathcal{I}_{\text{net}}$ discussed in Section 2.6 and listed in Table 1 is the area bounded by the temperature axis and the $\mathcal{I}^g$ curve.

value of 200 $m^2\ s^{-1}$. All ACCESS-OM2-1 configurations utilize a maximum (minimum) GM diffusivity of 600 $m^2\ s^{-1}$ (50 $m^2\ s^{-1}$) and a spatially constant neutral diffusivity of 600 $m^2\ s^{-1}$.

Sensitivity to the background vertical diffusivity is examined by comparing ACCESS-OM2-025 simulations with no background diffusivity, with a constant value of 10^{-5} $m^2\ s^{-1}$ and with a latitudinally dependent structure following Jochum (2009) with 5×10^{-6} $m^2\ s^{-1}$ in the mid- and high-latitudes reducing to 10^{-6} $m^2\ s^{-1}$ near the Equator. The background vertical viscosity is 10^{-4} $m^2\ s^{-1}$ in all simulations.

Sensitivity to the vertical resolution is evaluated by comparing five ACCESS-OM2-1 configurations with 50 to 135 vertical levels using two different level position schemes (see Table 1 and Section 5.3).

Finally, to test the impact of an increase in resolution in the absence of a strong reduction in the horizontal viscosity, we also examine an ACCESS-OM2-01-hvisc configuration where the lateral viscosity is kept at values more similar to ACCESS-OM2-025. Following Equations 12 and 13 of Griffies and Hallberg (2000), the grid-scale dependent biharmonic Smagorinsky viscosity coefficient is given by

$$B_{\text{smag}} = \frac{C^2\Delta^4}{8\pi^2}|D|, \tag{18}$$

where C is a dimensionless scaling parameter ($C = 2$ for all configurations in this article other than ACCESS-OM2-01-hvisc), Δ is the grid-scale and $|D|$ is the deformation rate of the horizontal flow. The presence of the flow-dependent deformation rate means that we cannot keep the viscosity exactly constant between the two configurations. If we assume that $|D|$ scales as Δ^{-1}, then to keep B_{smag} constant C should be increased proportional to $\Delta^{-3/2}$, and thus for ACCESS-OM2-01-hvisc we choose $C = 2\ (0.1/0.25)^{-3/2} \approx 7.9$. In reality $|D|$ increases only weakly with resolution when C is scaled in this manner, and thus B_{smag} in ACCESS-OM2-01-hvisc is still ∼50% less than in ACCESS-OM2-025 (however, in ACCESS-OM2-01 it is more than 15 times smaller).

4. Spatial Structure of Numerical Mixing in ACCESS-OM2-025

We start by examining properties of numerical mixing in the ACCESS-OM2-025 configuration. This configuration has the most numerical mixing across the model suite ($\mathcal{I}_{\text{net}} = 19.6$ PW °C, Table 1). Numerical mixing makes the dominant contribution to the globally integrated diathermal heat transport contributing, for example, 0.86 PW across the 21.5°C isotherm, which is 68% of the peak transport of 1.28 PW required to balance the surface forcing (compare black and blue lines in Figure 2). Indeed, numerical mixing is significant at all temperatures. The main features of the internal heat content budget shown in Figure 2 are consistent with the MOM025 Control simulation discussed by HZE19. ACCESS-OM2-025 has similar parameter settings to the zero background diffusivity simulation discussed by HZE19, which are also consistent with the parameter settings used in the ocean component of the GFDL CM2.5 climate model (Delworth et al., 2012 with an exception being the vertical grid; see Section 5.3).

In this section we discuss the spatial structure of the numerical mixing in ACCESS-OM2-025 using the diagnostic method discussed in Section 2. In Figure 3a–3c we show estimates of the heat flux through the 22.5°C, 15°C and 5°C isotherms due to numerical mixing averaged over 10 years in ACCESS-OM2-025. The numerical mixing heat flux has substantial spatial variability with hot-spots in the eddying WBCs and the ACC, near the continental shelves and slopes, and in the tropical thermocline. The flux is dominantly down-gradient as expected given the flux limiters on the advection scheme. However, there are notable regions with up-gradient fluxes, which are discussed in Appendix A (Section A3). The zonal mean structure highlights in particular the WBC and ACC regions (Figure 4), as well as the fact that numerical mixing is

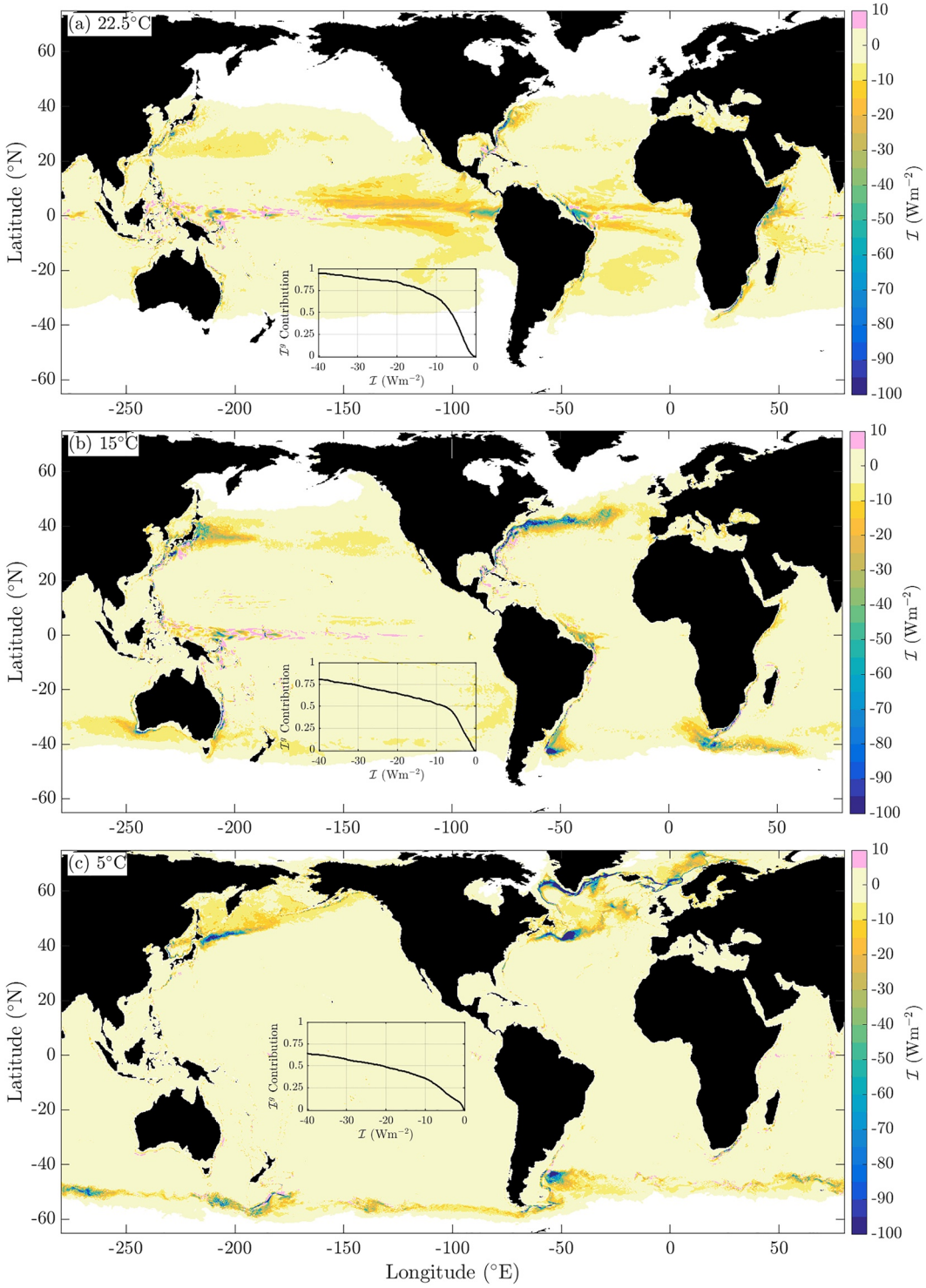

Figure 3. Fig Heat flux due to numerical mixing, $\mathcal{I}$ (W m^{-2}), through the (a) 22.5°C; (b) 15°C and (c) 5°C isotherms in ACCESS-OM2-025. The color interval is 5 W m^{-2} and positive up-gradient fluxes greater than 5 W m^{-2} are shown in pink. The inset panels indicate the cumulative contribution of different $\mathcal{I}$ flux values (in Wm^{-2}) to the global integral on the respective isotherm, $\mathcal{I}^g$. I.e. the y-axis is $D(\mathcal{I}) \equiv \int_0^{\mathcal{I}} \text{sort}(\mathcal{I}) dA \; / \; \mathcal{I}^g$, where sort($\mathcal{I}$) indicates a sorting of the $\mathcal{I}$ map from smallest to largest values. For example, in panel c, 50% of the total transport of heat across the 5°C isotherm is associated with fluxes less than −20 W m^{-2}. Note that the cumulative distributions in the inset panels are calculated from maps conservatively re-gridded to a 2.5°×2.5° grid (see Section A3 and Figure A1) and that the x-axis has been restricted to focus only on smaller values of $\mathcal{I}$ (the distribution reaches 1 for values of $\mathcal{I}$ more negative than −40 W m^{-2}).

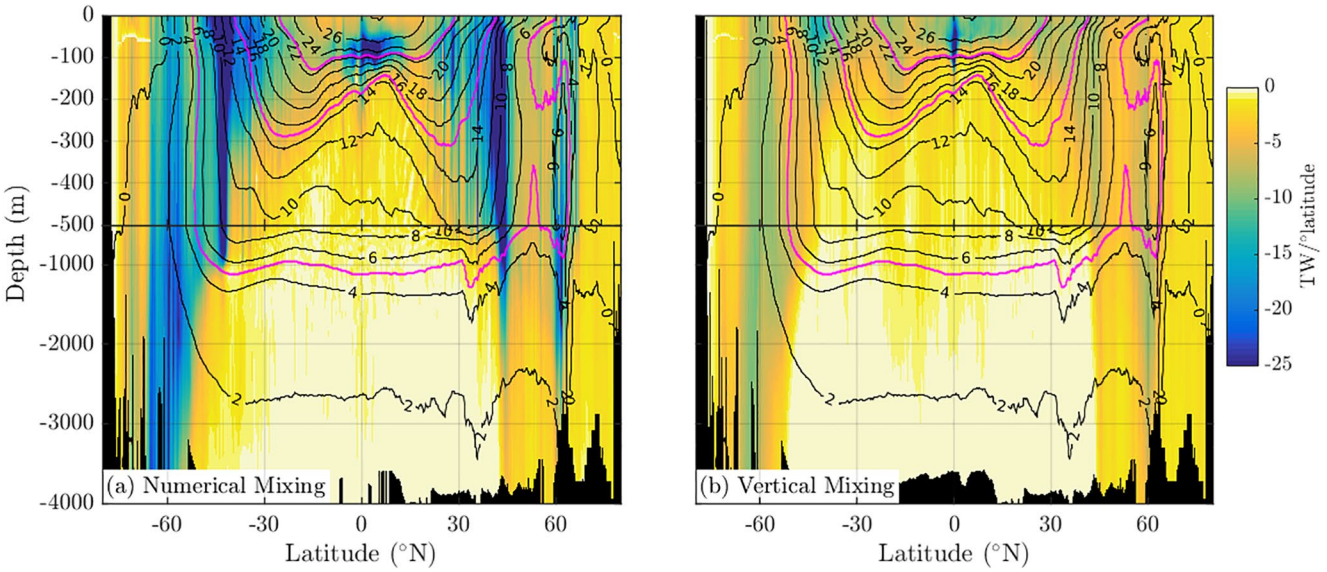

Figure 4. Zonally integrated across-isotherm heat fluxes due to (a) numerical mixing and (b) vertical mixing in ACCESS-OM2-025. The zonal-integral is performed following isotherms and then remapped to depth using the annual- and zonal-mean isotherm positions (black contours). This remapping should be kept in mind while interpreting the spatial structure. The 22.5°C, 15°C and 5°C isotherms on which spatial maps are shown in Figure 3 are contoured in magenta.

larger than explicitly parameterized vertical mixing throughout much of the ocean (compare Figure 4a and 4b), consistent with Figure 2.

4.1. Warm Temperatures

At warm temperatures (e.g., 22.5°C, Figure 3a) numerical mixing is particularly strong and extensive in the thermocline of the central and eastern tropical Pacific and the tropical Atlantic. The most intense fluxes are located east of the Galapagos in the Pacific and along the western boundary in the Atlantic. In both basins there are tongues of high mixing on either side of the Equator within the thermocline. These regions are characterized by strong grid-scale vertical and horizontal temperature gradients (Figure 5c and 5e) which numerical mixing acts to smooth (creating large down-gradient heat fluxes). Horizontal grid-scale velocity differences are also large, reaching root-mean-square values of 0.05 m s^{-1} in these regions (Figure 5a). This grid-scale variability in the horizontal velocity may be a major driver of the numerical mixing diagnosed in this region. The reason is that noise in the horizontal velocity translates into a noisy vertical velocity through continuity, and thus to noisy vertical advection across the thermocline (Ilicak et al., 2012). While here we focus on grid-scale variability, it should be noted that numerical errors could influence scales well above the grid-scale depending on the order of the schemes used (e.g., Soufflet et al., 2016).

Grid-scale noise in the horizontal velocity field can arise from numerical instabilities of the centered second-order momentum advection scheme (Leonard, 1984), momentum advection-diffusion (Bryan et al., 1975) or physical instabilities such as baroclinic instability acting near the grid scale (particularly at eddy-permitting resolution). Ilicak et al. (2012) proposed the grid Reynolds number as a proxy for the levels of spurious mixing, with sufficiently large viscosity needed to damp grid-scale horizontal velocity variability, reduce noisy vertical velocities and thus render small spurious mixing. However, when calculated using the square-root of the total kinetic energy (divided by ρ_0) as the velocity scale, we found that spatial variability in the biharmonic grid Reynolds number was not representative of the spatial structure in numerical mixing (not shown). This result might be because the grid Reynolds number does not include any direct measure of temperature variance on which numerical mixing depends. It might also signal that the total kinetic energy is not as relevant a velocity scale for numerical mixing as the eddy kinetic energy or a measure of the grid-scale horizontal velocity variance (or more generally, horizontal

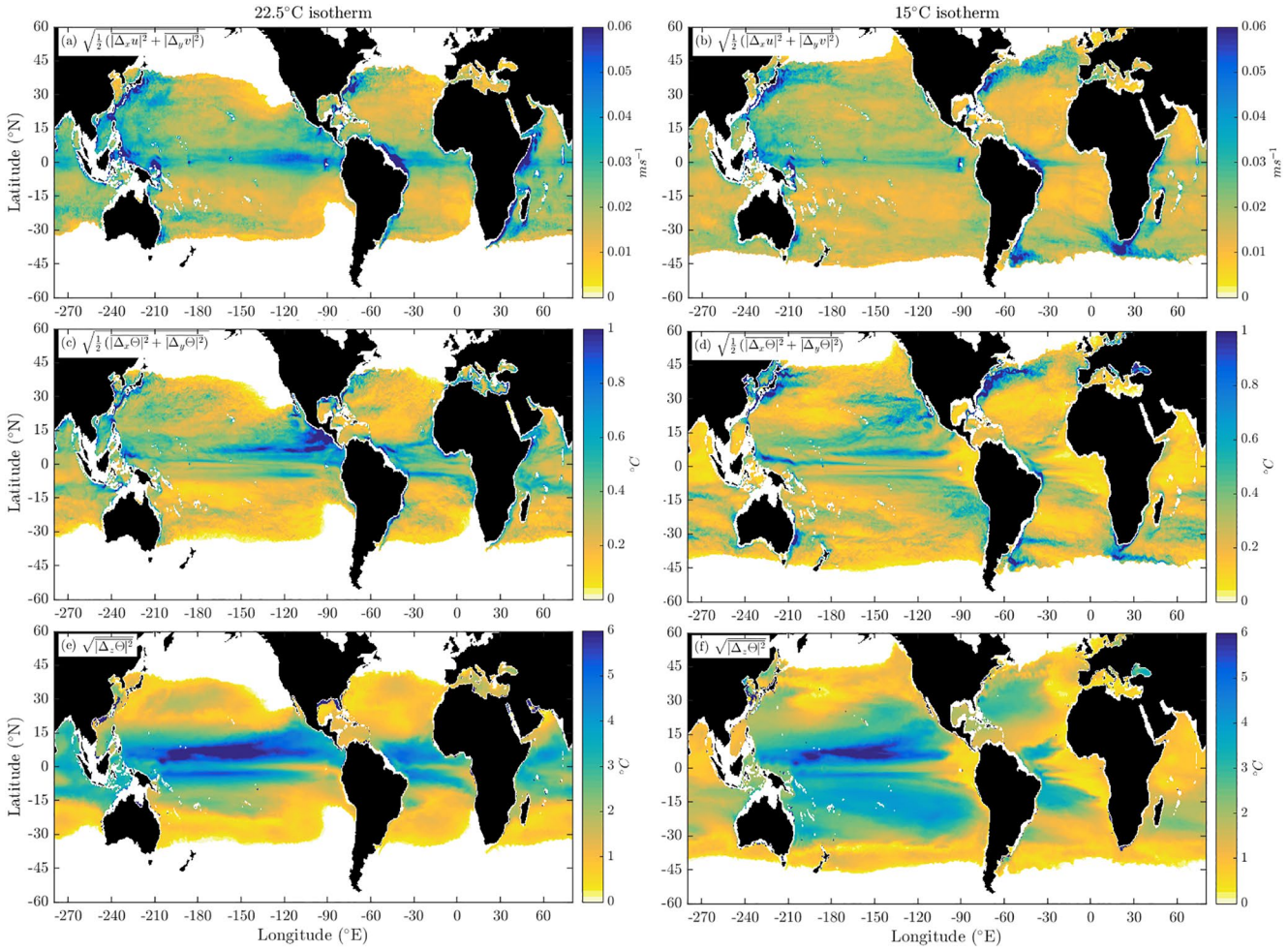

Figure 5. Root-mean-square (a and b) horizontal velocity grid cell differences, (c and d) horizontal temperature grid cell differences and (e and f) vertical temperature grid cell differences on the (a, c, and e) 22.5°C and (b, d, and f) 15°C isotherms from ACCESS-OM2-025. These quantities are calculated by taking the square of the difference in the specified direction (Δ_x, Δ_y or Δ_z) of the specified quantity (*u, v or Θ*) at each time step, time-averaging over a month, interpolating onto the monthly averaged isotherm and then taking the long-term time-average and square-root. Note that the colormaps saturate at high values.

velocity *gradients*). As an indicator of potential for numerical mixing, we choose to focus directly on the grid-scale horizontal velocity and temperature variances as an indication of noise in the solutions (e.g., Figure 5).

Numerical mixing along the Equator in the Pacific is strongest east of the Galapagos where the thermocline is particularly sharp and lies close to the surface (Figure 6a). This region is correlated with strong horizontal grid-scale temperature differences (Figure 6d). Weaker but more extensive levels of numerical mixing reaching 15 W m^{-2} are also found in the upper 100 m (generally above the thermocline, Figure 6a). Some of this numerical mixing occurs in the vicinity of the highly sheared upper Equatorial Undercurrent coinciding with the peak in explicitly parameterized vertical mixing associated with shear instability (compare Figure 6a and 6b, also see HZE19). This region is characterized by enhanced grid-scale horizontal velocity gradients (Figures 6c and 5a) likely associated with eddying flows such as Tropical Instability Waves (TIWs). TIWs are known to create strong fronts and both temperature and velocity variability in models and observations that influences turbulent mixing in the region (e.g., Warner et al., 2018). It is conspicuous that numerical mixing is restricted to isotherms that generally lie in the upper 100 m where grid-scale horizontal velocity differences (and TIW variability) are strongest and above the strong vertical temperature gradients in the thermocline. This pattern suggests that numerical mixing is unlikely to be associated exclusively with vertical advective processes. Note also that the numerical mixing in the

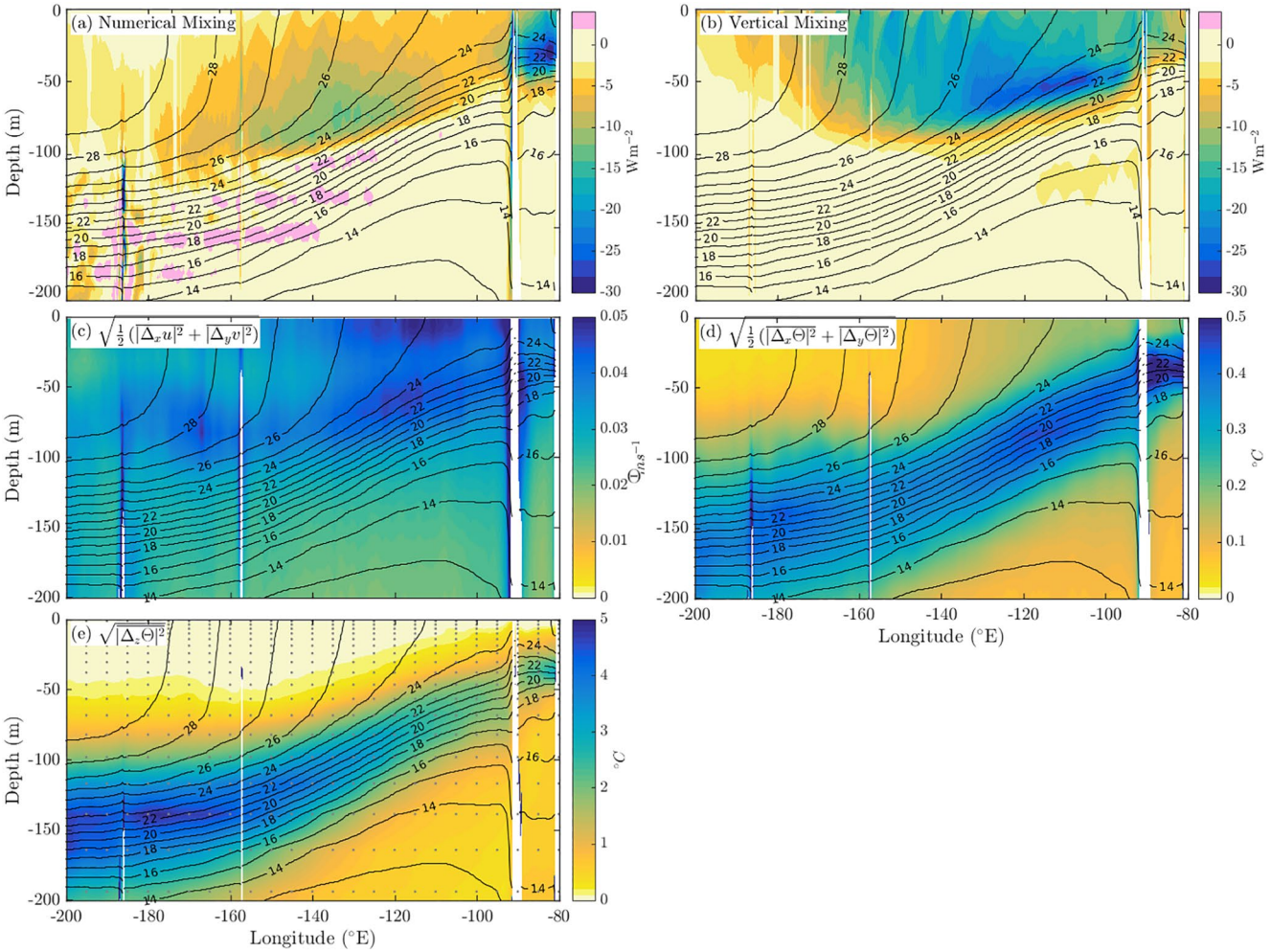

Figure 6. Longitude-depth slices between ± 2° of the Equator in the eastern Pacific of the (a) numerical mixing and (b) vertical mixing heat flux across isotherms from ACCESS-OM2-025. The heat flux is averaged in temperature coordinates and then remapped to depth using the annual-mean isotherm depths. The color interval is 2 W m^{-2} and positive up-gradient fluxes greater than 2 W m^{-2} are shown in pink. Root-mean-square (c) horizontal velocity grid cell differences, (d) horizontal temperature grid cell differences and (e) vertical temperature grid cell differences. The gray dots in panel e show the vertical grid locations of the KDS50 grid used in ACCESS-OM2-025.

equatorial regions exhibits a seasonal cycle consistent with the seasonal cycle in equatorial trade winds, current shear and TIWs (e.g., see Figure 11b of HZE19). While further study is required to evaluate the specific causes of numerical mixing in this region, some insight will be provided by parameter sensitivity tests in Section 5.

While we cannot isolate the diapycnal and isopycnal components of numerical mixing, the dominance of density variations by temperature in the tropics suggests that much of the numerical mixing in this region is diapycnal. This numerical mixing contributes to the too-diffuse vertical temperature gradients that characterize many models and have been implicated in SST biases such as the equatorial cold tongue bias or eastern upwelling region warm biases in global climate models (e.g., Richter, 2015 also see Section 5.2). These biases also impact the dynamics of the El Niño-Southern Oscillation (Meehl et al., 2001).

4.2. Cold Temperatures

At colder temperatures (e.g., 15°C and 5°C, Figures 3b, 3c and 4) numerical mixing is most prominent in the eddy-rich WBCs and the ACC. At 15°C the numerical mixing in the North Atlantic stretches along the

length of the Gulf Stream and its extension across the basin. In the zonal mean, these regions of strong numerical mixing descend to 1,000–1,500 m depth and are coincident with the regions of strong meridional temperature gradients (Figure 4a). These regions are characterized by large horizontal grid-scale temperature and horizontal velocity differences (Figure 5b and 5d). In contrast, the vertical grid-scale temperature differences in these regions do not stand out (Figure 5f). Thus, numerical mixing in these regions is likely associated with lateral mesoscale eddy stirring that creates strong horizontal temperature gradients near the grid-scale that are subsequently smoothed by the advection operator. This process mimics the real ocean equivalent of a downscale cascade of temperature variance along neutral directions by mesoscale stirring toward its ultimate dissipation at small scales through irreversible mixing (e.g., McDougall et al., 2014; Smith & Ferrari, 2009). In ACCESS-OM2-025, where there is no physically imposed lateral diffusive closure, the numerical mixing acts as a surrogate for small-scale diffusion by dissipating the gradients near the grid-scale. This approach is consistent with the implicit Large Eddy Simulation (implicit LES) approach pursued for certain three-dimensional turbulence studies (Margolin et al., 2006). However, it is unclear whether such an approach is physically suitable or robust in the case of isopycnal diffusion.

In addition to the eddying WBCs, there are some contributions from topographic hot spots around the continental shelves (e.g., around Australia in Figure 3b). At warmer temperatures these regions make a minor contribution to the global transport. However, at 5°C there are large fluxes around the continental shelves in the high-latitude North Atlantic (Figure 3c). These continental slope regions are once again characterized by strong horizontal grid-scale temperature and horizontal velocity differences (e.g., Figure 5b and 5d). The numerical mixing along the high-latitude continental shelves and slopes may have an impact on bottom water formation through interior water-mass transformation (e.g., MacGilchrist et al., 2020).

While Figure 3 indicates sites of intense numerical mixing associated with the equatorial regions, WBCs and continental shelves, it should be noted that weak fluxes over large areas also make significant contributions to the total diathermal heat transport $\mathcal{I}^g$. For example, 50% of the total heat transport across the 22.5°C isotherm is associated with fluxes of less than ~7 Wm^{-2} (inset in Figure 3a). The contribution of weak fluxes over large areas is smaller for colder isotherms (e.g., for the 5°C isotherm 50% of the total heat transport is supplied by fluxes greater than 20Wm^{-2}, inset in Figure 3c), which might be because thermal gradients are weaker in the interior on colder isotherms.

5. Sensitivity to Model Parameters

In this section we examine the sensitivity of numerical mixing to various model parameters. The global-average diathermal heat budgets for each configuration are shown together in Figure 7, with numerical mixing in panels i and j. The globally integrated summary diagnostic $\mathcal{I}_{\mathrm{net}}$ discussed in Section 2.6, being the area bounded by the temperature axis and the $\mathcal{I}^g$ curve in Figure 7i and 7j, is listed in Table 1. We consider the impact of varying explicit neutral physics parameterizations (Section 5.1), background vertical diffusivity (Section 5.2), vertical resolution (Section 5.3), lateral viscosity (Section 5.4) and horizontal resolution (Section 5.5).

Changes in model parameters or resolution can impact the global diathermal heat budget shown in Figure 7 in a number of interacting ways. For example, changes in physical mixing parameters alter the temperature structure of the solution. This change in temperature structure can impact on numerical mixing (Figure 7i and 7j), for example through reduced gradients for the numerical mixing to act on. Feedbacks then can project onto the physical mixing itself as well as the surface forcing (Figure 7a and 7b) through changes in the SST or upper-ocean thermal structure into which those surface fluxes enter. Here we focus on semi-equilibrated simulations meaning that differences measured between simulations are the result of a chain of feedbacks.

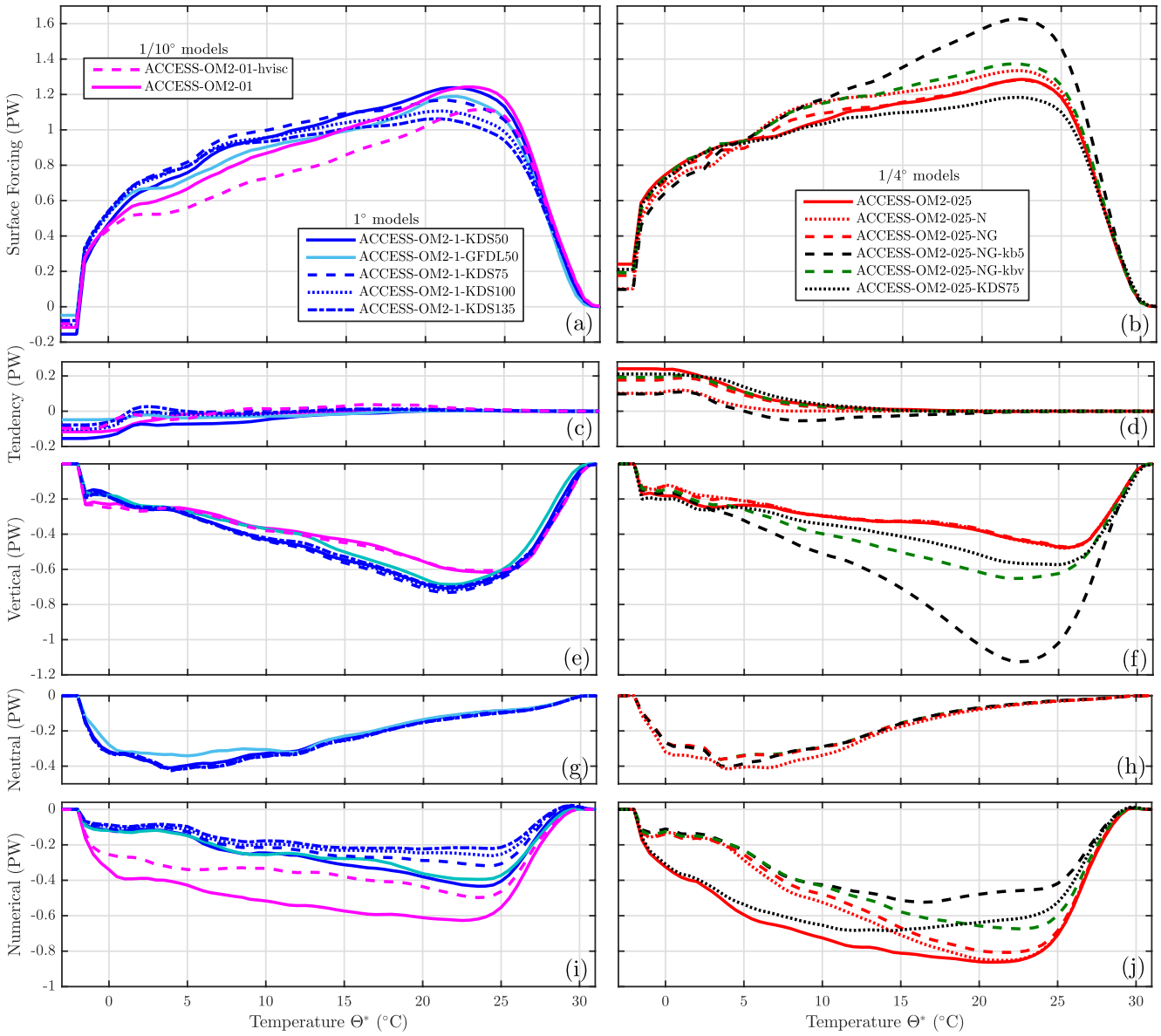

Figure 7. The global annually averaged diathermal heat budget (Equation 9) across the suite of model simulations. (a and b) Surface forcing $\mathcal{F}^g + \mathcal{P}_I^g$, (c and d) the internal heat content tendency $\partial \mathcal{H}_I^g / \partial t$, (e and f) explicitly parameterized vertical diffusion $\mathcal{M}^g$, (g and h, if present) explicitly parameterized neutral diffusion $\mathcal{N}^g$ and (i and j) numerical mixing $\mathcal{I}^g$. Note that the vertical scale of every panel is the same to facilitate comparison. The global metric $\mathcal{I}_{\text{net}}$ discussed in Section 2.6 and listed in Table 1 is the area bounded by the temperature axis and the $\mathcal{I}^g$ curve in panels (i and j).

5.1. Neutral Physics

As discussed in Section 4, at cold temperatures numerical mixing is largely associated with the eddying WBCs and ACC (e.g., Figure 3b and 3c), where at 1/4° and finer grid spacing large lateral temperature gradients are created by along-isopycnal mesoscale eddy-stirring (e.g., Figure 5d). Here, we hypothesize that the diathermal heat flux arising from numerical mixing is linked to isopycnal and lateral processes.

In ACCESS-OM2-025 as well as the 1/10° ACCESS-OM2-01 configuration, no parameterization for lateral or neutral mixing are included in the tracer equation. This choice, also made for the MOM025 configurations considered by HZE19, was made to maximize the preservation of isopycnal tracer gradients at the scales admitted by the models, as well as to remove the need to tune these rather complex physical closures in expensive model configurations. As a result, the tracer advection scheme is left to smooth tracer gradients

near the grid scale and allow the model to make the most of its resolution as per the implicit LES approach (Margolin et al., 2006). This approach comes with the important caveats that, depending on the advection scheme, numerical mixing may also affect scales above the grid-scale and is not constrained to follow the same physical laws as physical diffusion. Here, we examine the interplay between the numerical and parameterized eddy parameterizations by comparing ACCESS-OM2-025 (no neutral diffusion nor GM eddy-induced advection); ACCESS-OM2-025-NG (both neutral diffusion and the GM eddy-induced advection enabled); and ACCESS-OM2-025-N (with neutral diffusion yet no GM advection) (red lines in Figure 7b, 7d, 7f, 7h, and 7j).

When neutral diffusion and the GM parameterizations are both turned on, numerical mixing reduces between −1°C and 25°C (compare red solid and red dashed lines in Figure 7j), with the strongest impact being between −1°C and 15°C where the diathermal heat transport due to parameterized neutral diffusion in ACCESS-OM2-025-NG peaks (dashed red line in Figure 7h). These changes are largely due to the presence of parameterized neutral diffusion, with the presence or absence of the GM scheme having a smaller impact given the magnitude of the GM diffusivity that has been chosen in ACCESS-OM2-025-NG. Both heat fluxes due to neutral diffusion and due to numerical mixing are slightly enhanced when GM is turned off (compare dotted and dashed red lines in Figure 7h and 7j). The replacement of parameterized neutral diffusion with enhanced numerical mixing and vice versa appears relatively benign with respect to the global diathermal heat budget, with only small changes in the surface forcing, tendency or vertical diffusion terms (compare red solid and dashed lines in Figure 7b, 7d, and 7f).

While the neutral diffusivity is scaled by the ratio of the grid spacing and the Rossby radius of deformation (it has values of less than 20 $m^2\ s^{-1}$ in the tropics where the Rossby radius is better resolved, while reaching 200 $m^2\ s^{-1}$ at high-latitudes and over shallow shelves), tests with an older configuration that utilized a constant neutral diffusivity of 300 $m^2\ s^{-1}$ showed only a small further reduction in numerical mixing (not shown). Changes of less than 0.02 PW occurred at temperatures warmer than 20°C, suggesting again that numerical mixing at warmer temperatures in the tropics is associated with diapycnal, and not isopycnal, processes. Instead, the changes in numerical mixing occur nearly exclusively in the WBCs, ACC and high-latitude continental shelves/slopes where eddy-variability dominates (Figure 8). While in most of these areas numerical mixing shows an overall reduction when neutral diffusion is introduced, there are also some localized regions where numerical mixing is increased due to shifts in the location of mean currents and eddy pathways (e.g., north of the Gulf Stream in Figure 8b and 8d).

As a representative region, we examine changes in the Gulf Stream extension in more detail (Figure 9). In this region there is a broad reduction of numerical mixing in ACCESS-OM2-025-NG and ACCESS-OM2-025-N across the 2°C–20°C range, peaking at a ∼40% reduction near 10°C (Figure 9a). This reduction in numerical mixing is associated with a reduction in Eddy Kinetic Energy (EKE), resolved eddy-driven stirring and therefore horizontal grid-scale velocity and temperature differences (Figure 9b–9d). Changes in vertical grid-scale temperature differences are less coherent (Figure 9e). While the GM scheme has a larger impact on horizontal grid-scale velocity differences (Figure 9c), neutral diffusion has the dominant impact on horizontal grid-scale temperature differences. These changes in horizontal grid-scale temperature differences appear to drive the majority of the changes in numerical mixing (Figure 9a). These results support the conclusion that in active mesoscale eddying regions the dominant driver of numerical mixing is grid-scale noise in the horizontal velocity and temperature fields (e.g., Ilicak et al., 2012). Neutral diffusion reduces numerical mixing by smoothing horizontal grid-scale temperature differences, while the GM scheme drives a small further reduction in numerical mixing by reducing horizontal velocity variability. However, while numerical mixing is reduced when these parameterizations are turned on, other changes in the simulations, such as reduced eddy activity, emphasize that it remains an open question as to whether it is better to dissipate grid-scale temperature gradients through numerical or physical mixing. These two mixing processes may not be expected to have the same impact on the simulation.

5.2. Background Vertical Diffusivity

As discussed in HZE19, there is an interplay between the physically based vertical mixing and the numerical mixing. When the physically based vertical diffusivity is increased, small-scale vertical gradients in

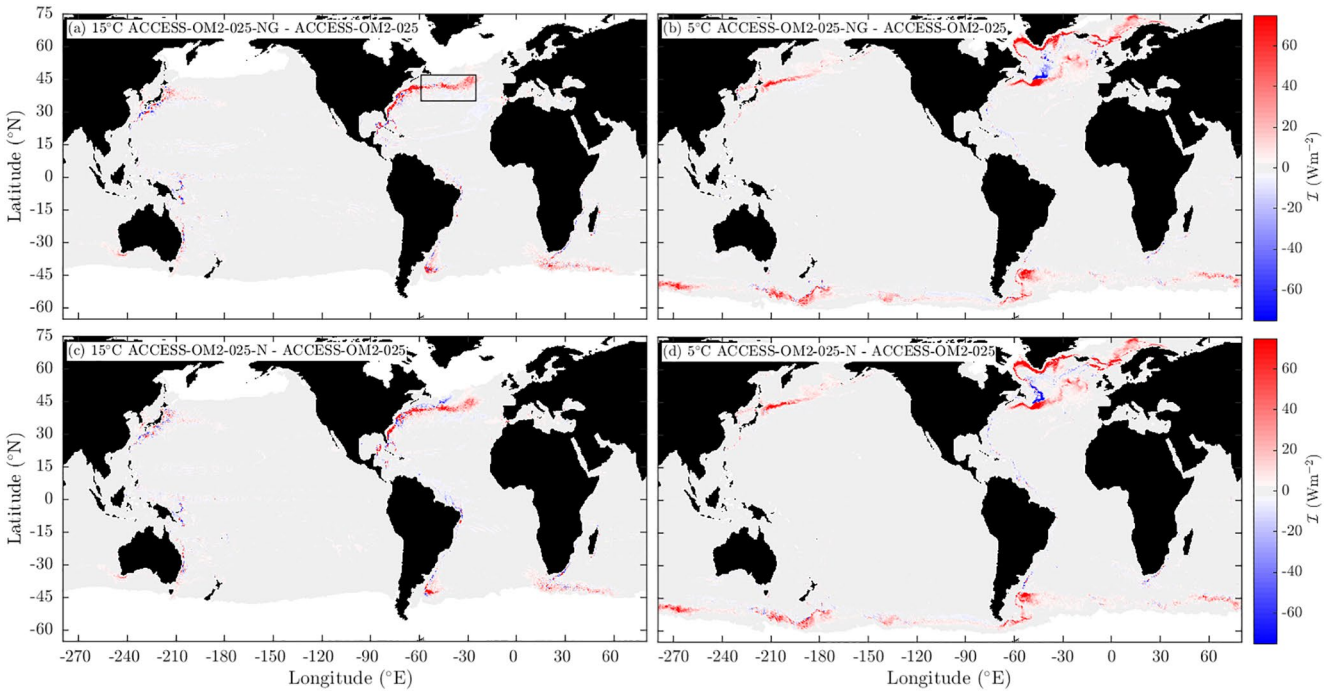

Figure 8. Difference in the diathermal heat flux due to numerical mixing through the (a and c) 15°C and (b and d) 5°C isotherms in the (a and b) ACCESS-OM2-025-NG with both neutral diffusion and the GM parameterization and (c and d) ACCESS-OM2-025-N with only neutral diffusion compared with ACCESS-OM2-025 which has neither (the ACCESS-OM2-025 totals are shown in Figure 3b and 3c). Red (blue) indicates a decrease (increase) in the magnitude of down-gradient numerical diffusion when the respective parameterizations are turned on. The black box in panel a indicates the Gulf Stream extension region analyzed in Figure 9.

temperature are decreased and therefore numerical mixing, if linked with vertical advective processes, will decrease (in addition to secondary feedbacks to the circulation). This mechanism is evident when comparing the ACCESS-OM2-025-NG configurations which differ only in their background vertical diffusivity, particularly at temperatures above 10°C (compare red, black and green dashed lines in Figure 7b, 7d, 7f, and 7j). Increasing the background vertical diffusivity from 0 to 10^{-5} m^2 s^{-1}, a typical background value used in many climate models, more than doubles the peak diathermal heat transport due to vertical mixing between 20°C and 25°C. However, the resultant change in the total diathermal heat transport (that which balances the surface forcing, compare dashed lines in Figure 7b) is less than that expected from the changes in vertical mixing alone (dashed lines in Figure 7f), due to compensation by changes in numerical mixing (dashed lines in Figure 7j). Numerical mixing is decreased by approximately a factor of two when the 10^{-5} m^2 s^{-1} background diffusivity is turned on (compare black and red dashed lines in Figure 7j).

On the 22.5°C isotherm, near the peak of the diathermal heat transport, the changes in numerical mixing occur primarily in the tropical thermocline (Figure 10a), particularly in the eastern Pacific and Atlantic where the thermocline is sharp and background diffusion can drive large diathermal heat fluxes (e.g., see HZE19, their Figure 4b). Given that temperature dominates density variability in the tropics, the changes in numerical mixing as the vertical diffusivity is changed supports the conclusion that the numerical mixing in these regions is diapycnal. There are also some changes in the mid-latitude interior where background diffusion is replaced by numerical mixing when the background diffusivity is set to zero. This is consistent with the fact that the background diffusivity has a stronger damping effect on weak, large-area fluxes than on regions of intense fluxes (compare solid and dashed lines in inset in Figure 10a). There is little consistent change in numerical mixing in the WBCs or continental slopes and shelves, supporting the conclusion made in the previous section that numerical mixing in these regions is associated with lateral rather than vertical processes. Consequently, at cold temperatures the dependence of numerical mixing on the background vertical diffusivity is weak despite significant changes in the diathermal heat transport due to vertical mixing (compare dashed lines in Figure 7f and 7j).

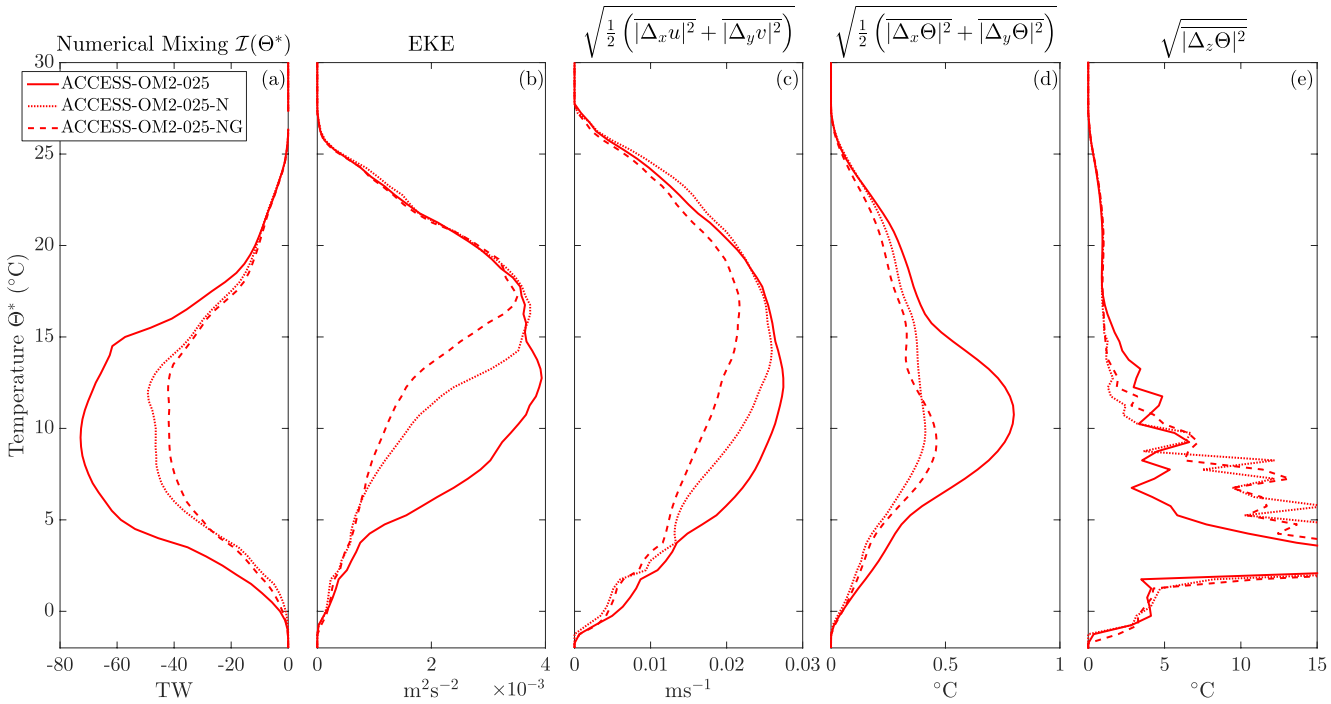

Figure 9. Differences in numerical mixing and grid-scale horizontal velocity and temperature differences in the Gulf Stream extension (59°W–25°W, 35°N–47°N, black box in Figure 8a). (a) Diathermal heat transport due to numerical mixing $\mathcal{I}(\Theta)$, (b) sub-monthly Eddy Kinetic Energy (EKE) and root-mean-square grid-scale (c) horizontal velocity, (d) horizontal temperature and (e) vertical temperature differences. The quantities in panels (b–e) are interpolated onto isotherms using monthly averaged temperature and then spatially and temporally averaged.

Focusing on a region in the Eastern Tropical Pacific (black box in Figure 10a), the background diffusivity has little influence on horizontal velocity variability or grid-scale differences (Figure 11b and 11c). However, the expected reduction in grid-scale vertical temperature differences when the background diffusivity is increased is also accompanied by a similar factor reduction in horizontal grid-scale temperature differences (Figure 11d and 11e). This result suggests that horizontal grid-scale temperature variability is created by small-scale vertical advection of the background vertical temperature gradient. Reducing this background vertical temperature gradient by increasing the vertical diffusivity reduces both horizontal and vertical temperature gradients at the grid-scale, in turn leading to a reduction in numerical mixing (Figure 11a).

The changes in background diffusivity have an impact on temperature biases in the equatorial Pacific thermocline (Figure 12a–12c). ACCESS-OM2-025-NG-kbv, with a background diffusivity of 10^{-6} m^2 s^{-1} at the Equator, shows a slightly smaller overall bias than the default configuration of ACCESS-OM2-025-NG (no background diffusivity) which has a strong cold bias below the thermocline, suggesting that the larger numerical mixing in ACCESS-OM2-025-NG does not compensate for reduced vertical mixing (i.e., a small explicit background vertical diffusivity is needed to reduce equatorial biases). In contrast, ACCESS-OM2-025-NG-kb5 (Figure 12c) is too warm nearly everywhere.

5.3. Vertical Resolution

Numerical mixing is also sensitive to the vertical grid resolution, here examined using a set of ACCESS-OM2-1 simulations. Most of the configurations in this article use the Stewart et al. (2017, denoted KDS) vertical levels scheme which has fine grid spacing in the upper ocean (nearing $1 - 2$ m near the surface, colored lines in Figure 13) in order to better resolve the vertical structure of baroclinic modes in shallow regions. We also consider a configuration with the 50 level grid (GFDL50) used in the ocean component of the GFDL CM2.5 climate model (Delworth et al., 2012), which has 10 m vertical grid spacing in the upper 200 m (black line in Figure 13).

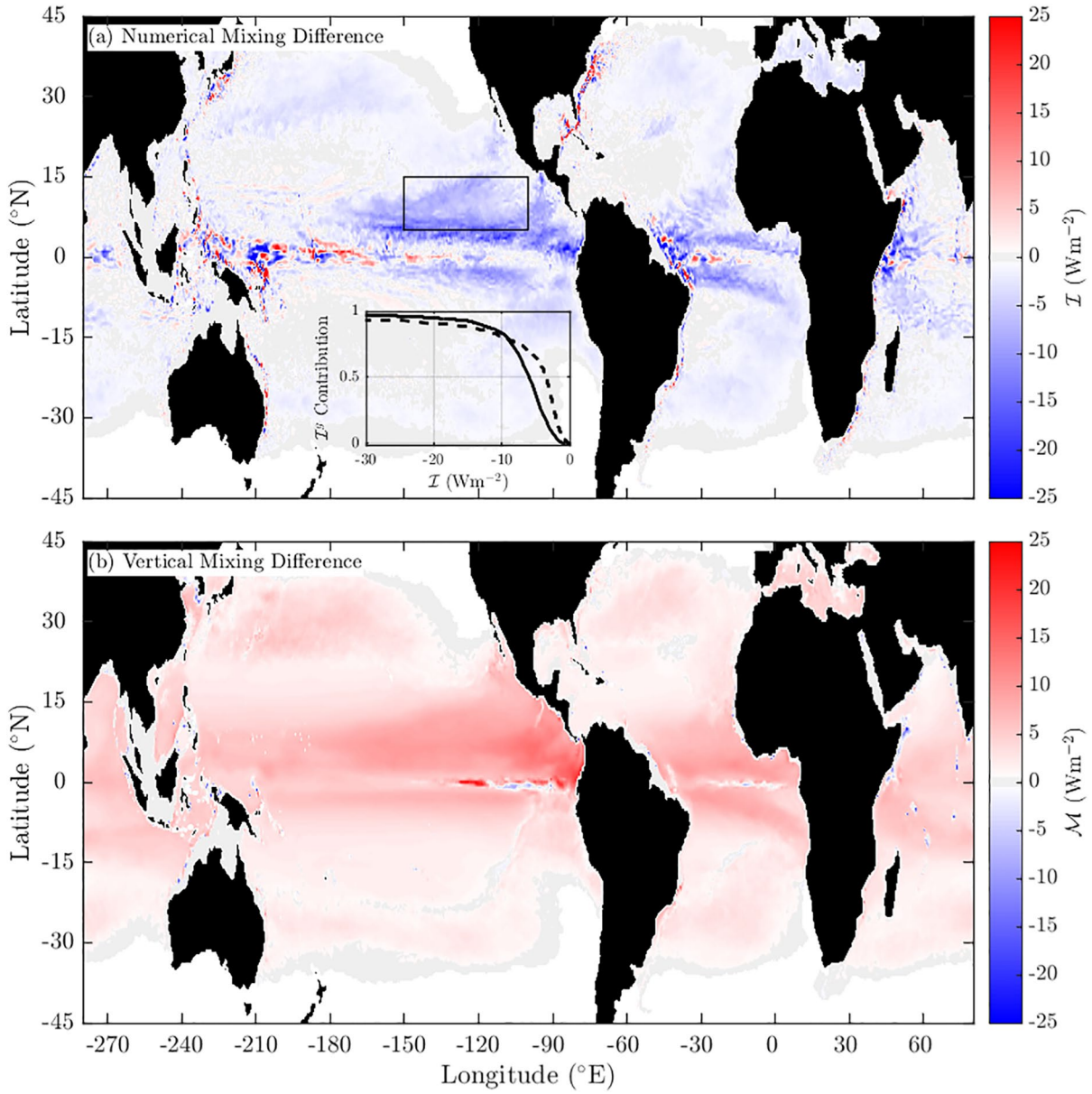

Figure 10. The difference between the heat flux across the 22.5°C isotherm due to (a) numerical mixing and (b) physically based vertical diffusion between the ACCESS-OM2-025-NG configuration with no background vertical diffusivity and the ACCESS-OM2-025-NG-kb5 configuration with a 10^{-5} m^2 s^{-1} background vertical diffusivity. Both numerical and vertical diffusive fluxes are negative (down-gradient), meaning that the blue regions in panel (a) signal an increase in the strength of numerical mixing in ACCESS-OM2-025-NG compared to ACCESS-OM2-NG-kb5 while the red regions in panel (b) signal a decrease in the strength of vertical mixing in ACCESS-OM2-025-NG compared to ACCESS-OM2-NG-kb5. The black box in panel (a) indicates the region analyzed in Figure 11. The inset in panel (a) indicates the cumulative contribution of different $\mathcal{I}$ flux values (in Wm^{-2}) to the global integral $\mathcal{I}^g$ for ACCESS-OM2-025-NG (dashed) and ACCESS-OM2-025-NG-kb5 (solid), as described in more detail in the caption of Figure 3.

The changes in vertical grid spacing have an impact on numerical mixing at most temperatures, with the largest changes between 15°C and 27°C (compare blue lines in Figure 7i). As for the background diffusivity, the dominant changes occur in the equatorial regions where the vertical temperature stratification is largest. An equatorial Pacific longitude-depth slice for each configuration is shown in Figure 14. In general, as the number of grid levels increases, the numerical mixing reduces. However, the placement of the levels also makes a difference. The KDS grid has a much finer vertical grid spacing near the surface (2.3 m in KDS50 and 1.1 m in KDS75 compared to 10 m in GFDL50, Figure 13), meaning that the sharp vertical gradients in the far eastern Pacific shallower than 50 m depth are better resolved by the KDS50 grid com-

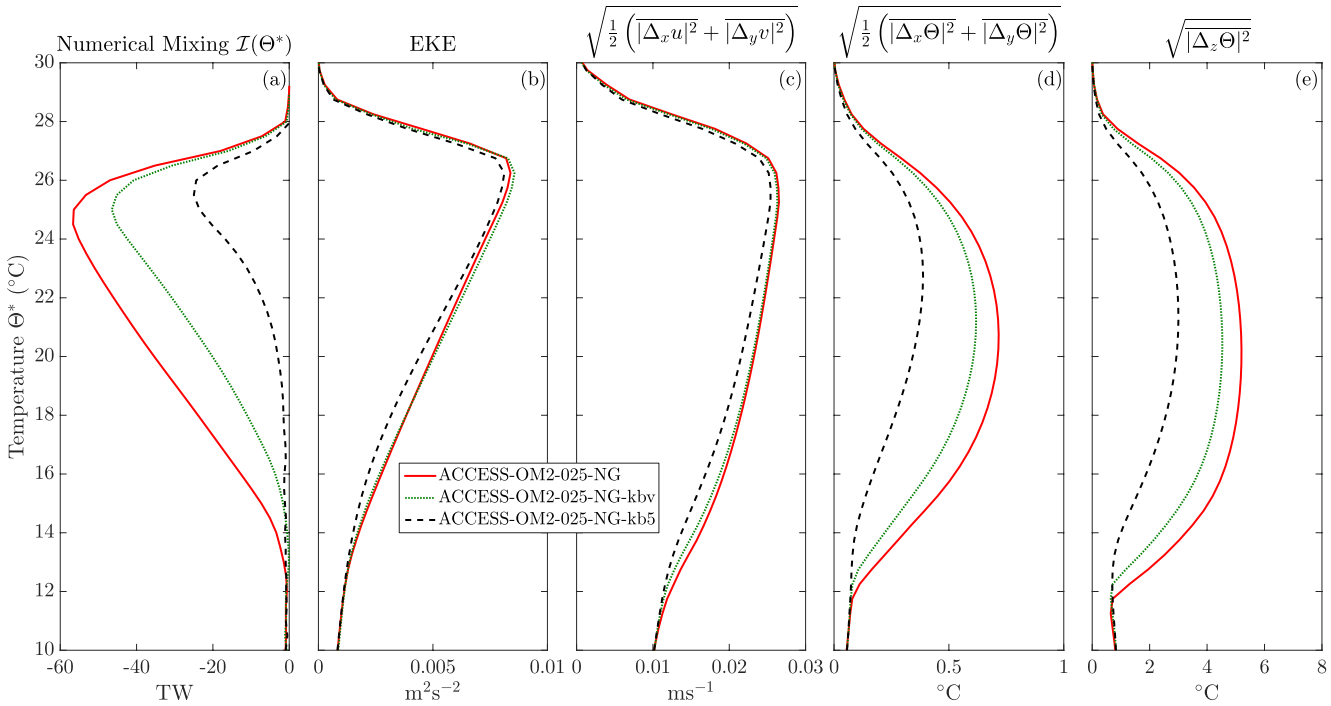

Figure 11. Analysis of the sensitivity of numerical mixing and grid-scale temperature and horizontal velocity differences to the background vertical diffusivity in the Eastern Tropical Pacific (150°W–100°W, 5°N–15°N, black box in Figure 10a). ACCESS-OM2-025-NG (red lines) has no background vertical diffusivity, ACCESS-OM2-025-NG-kb5 (black dashed lines) has a background vertical diffusivity of 10^{-5} m^2 s^{-1} and ACCESS-OM2-025-NG-kbv (green dotted lines) has a latitudinally dependent background vertical diffusivity of between 1×10^{-6} m^2 s^{-1} and 3×10^{-6} m^2 s^{-1} in this region. (a) Diathermal heat transport due to numerical mixing $\mathcal{I}(\Theta)$, (b) sub-monthly Eddy Kinetic Energy (EKE) and root-mean-square grid-scale (c) horizontal velocity, (d) horizontal temperature and (e) vertical temperature differences. The quantities in panels b–e are interpolated onto isotherms using monthly averaged temperature and then spatially and temporally averaged.

pared to the GFDL50 grid. Numerical mixing in ACCESS-OM2-1-GFDL50 here is much larger (compare Figure 14a and 14b east of −100°E). However, between 50 and 250 m depth the GFDL50 grid has a finer vertical grid spacing than KDS50 (compare black and blue lines in Figure 13) and so numerical mixing is lower in GFDL50 (compare Figure 14a and 14b in the central Pacific). This depth range corresponds to the thermocline where vertical temperature gradients are largest throughout most of the ocean, and so globally numerical mixing is slightly lower in ACCESS-OM2-1-GFDL50 than in ACCESS-OM2-1-KDS50 above ~13°C (compare light and dark blue lines in Figure 7i).

It is interesting to note that numerical mixing at cold temperatures is also sensitive to the vertical resolution, despite being insensitive to the background vertical diffusivity. These changes may be linked to the interplay between horizontal and vertical grid-scale temperature gradients in the presence of grid-scale horizontal velocity variability. However, we note that ACCESS-OM2-1 does not resolve eddy-variability.

In the KDS50 configuration there are some weak apparent up-gradient numerical mixing fluxes in the lower portion of the thermocline in the western and central Pacific (pink in Figure 14). As discussed in more detail in Appendix A, the use of flux limiters on the MDPPM advection scheme should maintain monotonicity in the advected tracer distribution and prevent up-gradient fluxes, suggesting that these apparent up-gradient fluxes may arise from limitations in our diagnostic method. These equatorial up-gradient fluxes are in a region where KDS50 has particularly coarse grid spacing - with only four vertical levels between 100 and 200 m (see dots in Figure 14a). The presence of a large number of isotherms within each single model vertical grid cell suggests that our method for quantifying numerical mixing may be sensitive to small vertical isotherm movements in this region (however, we note that for a given isotherm our method is not sensitive to the temperature binning resolution, here 0.5°C, as all quantities are integrated over all temperature bins warmer than a given isotherm, see also Appendix A). These weak up-gradient fluxes are present in all simulations that use the KDS50 grid (e.g., ACCESS-OM2-025, Figure 3a and 3b and

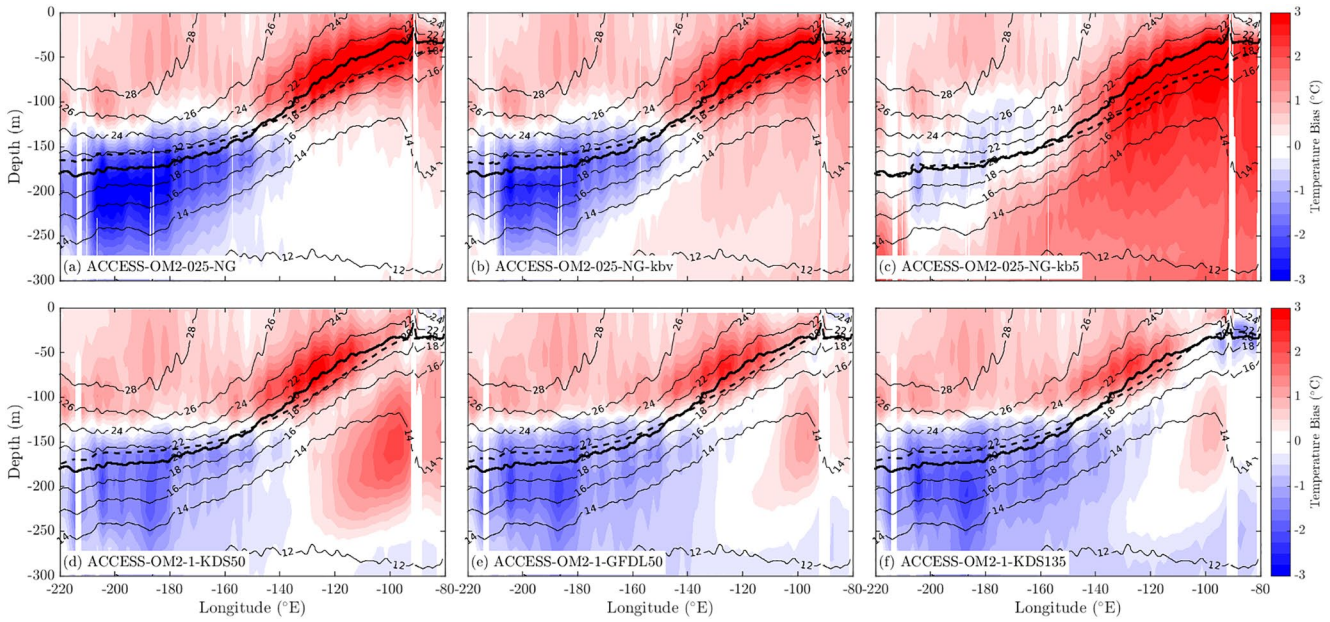

Figure 12. Equatorial Pacific depth-longitude temperature bias plots compared to WOA13 for (a–c) three ACCESS-OM2-025-NG configurations with differing background vertical diffusivity and (d–f) three ACCESS-OM2-1 configurations with differing vertical resolution. ACCESS-OM2-025-NG uses no background vertical diffusivity, ACCESS-OM2-025-NG-kb5 uses a background diffusivity of 10^{-5} m^2 s^{-1} and ACCESS-OM2-025-NG-kbv and the ACCESS-OM2-1 configurations use a background diffusivity of 10^{-6} m^2 s^{-1} on the Equator. The contours show the WOA13 isotherms with the 20°C isotherm in a thicker line. The thick dashed line is the position of the modeled 20°C isotherm.

Figure 6a) but not in configurations using the GFDL50 grid which has a finer grid spacing in this region (e.g., Figure 14b).

The default time step in ACCESS-OM2-1 is 1.5 h. However, using this time step apparent up-gradient fluxes of up to 5 W m^{-2} appear at the surface at warmer temperatures in the western Pacific in the KDS configurations where the grid spacing is very fine (not shown). Reducing the time step to 20 min for the diagnostic accumulation period (as used for all the ACCESS-OM2-1 simulations presented here) removes the majority of these apparent up-gradient fluxes. A comparison of the terms in the internal heat content budget between the fast and slow time step cases suggests that this apparent up-gradient mixing is linked to an underestimation of the transport of heat into the warmest temperatures classes from surface forcing (not shown). This under-estimation suggests that the rapid changes in near-surface stratification and solar penetrative heating over the diurnal cycle at time scales comparable to the 1.5 h time step cannot be properly captured by our online diagnostic binning (possibly because of the temporal discretization of the surface forcing and mixing flux convergence binning as discussed in Appendix A, Section A2). Note that apart from this dependence in ACCESS-OM2-1 we found little dependence of numerical mixing on time step. For example, ACCESS-OM2-025 simulations performed with the default time step of 1350 and 675 s showed little difference in numerical mixing metrics (this is reassuring as the time step is often changed during model spin-up to maintain stability). This insensitivity to the time step may arise because decreasing the time step decreases the numerical diffusivity (which may be proportional to Δt for a simple forward time stepping scheme) but increases the magnitude of the time derivative so that the net change is negligible.

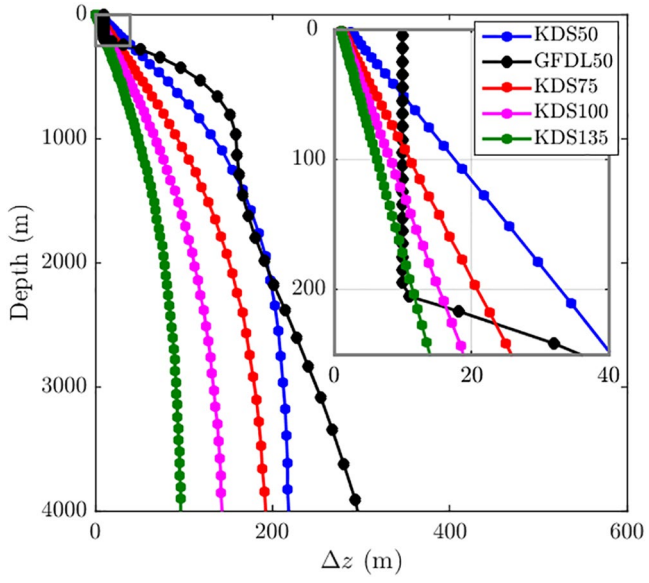

Figure 13. The vertical grid spacing Δz as a function of depth for the five vertical grids used in this study. The inset shows a zoom on the upper 250 m (gray box).

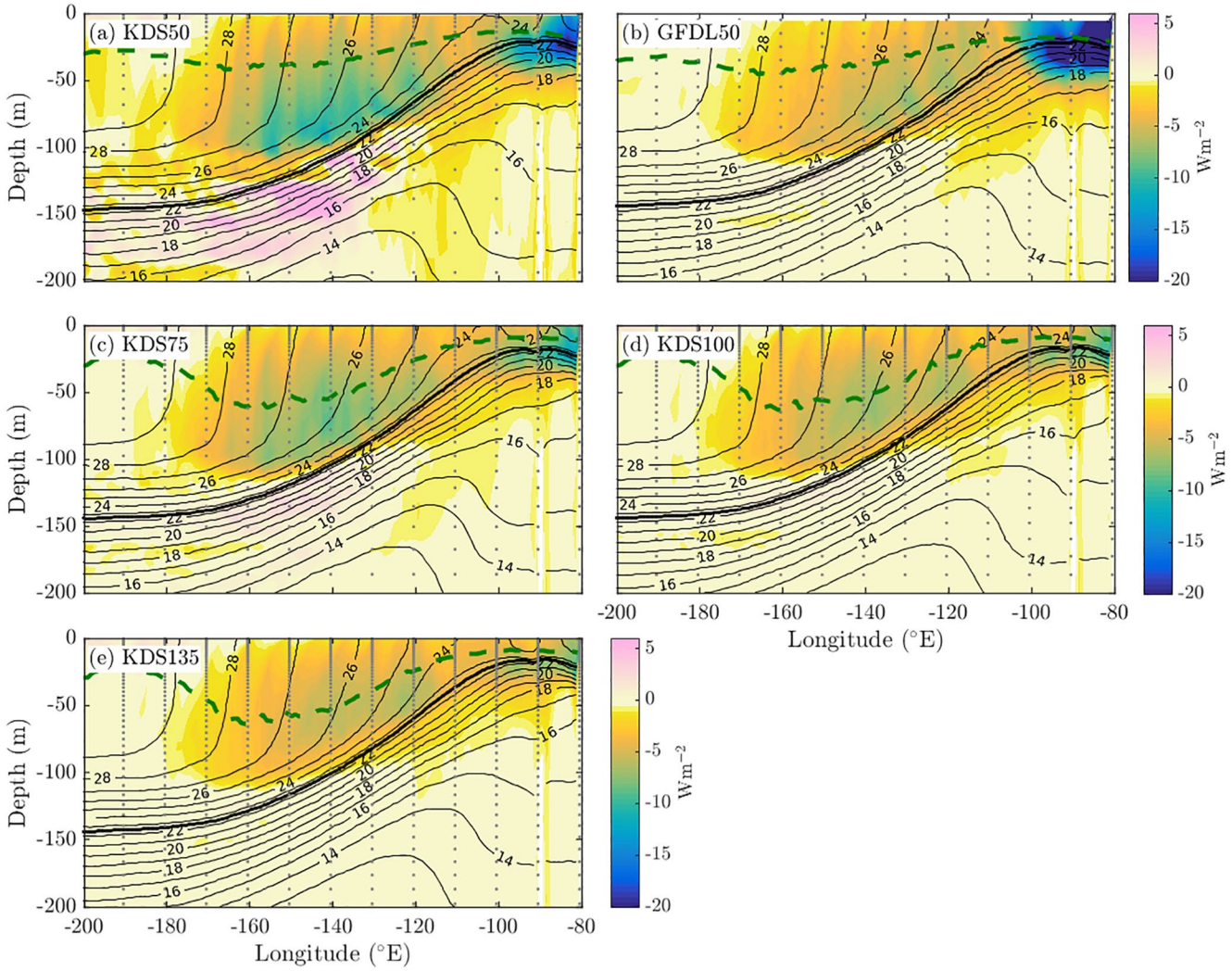

Figure 14. Equatorial longitude-depth slices of the numerical mixing heat flux across isotherms averaged within ±2° of the Equator in the ACCESS-OM2 1-degree runs from the coarse (a) KDS50 and (b) GFDL50 configurations to the fine (e) KDS135. The heat flux is averaged in temperature coordinates and then remapped to depth using the annual-mean isotherm depths (contours). Positive up-gradient fluxes are shown in pink shades. The green dashed line indicates the mixed layer depth determined from a 0.032 kg m^{-3} density criterion and the gray dots plotted every 10° longitude indicate the vertical grid level locations.

Unlike the impact of a changing background vertical diffusivity, the changes in numerical mixing with vertical grid spacing do not appear to be compensated by changes in either vertical or neutral diffusion (Figure 7e and 7g). Instead, the reduction in numerical mixing results in a change in the surface temperature structure and surface fluxes such that the net diathermal heat transport is altered (blue lines in Figure 7a). The changes in vertical grid spacing impact the temperature structure in the equatorial Pacific. Finer grids reduce the consistent warm biases at depth in the eastern Pacific by sharpening the thermocline, although at the cost of a slight cold bias in the upper eastern Pacific and a slightly increased cold bias in the deep western Pacific in ACCESS-OM2-1-KDS135 (compare Figure 12d–12f). These results highlight the need to consider the interplay between vertical resolution, vertical background diffusivity and numerical mixing together when making parameter choices. We also see differences at higher latitudes and colder temperatures (Figure 7i), where Stewart and Hogg (2019) showed that surface fluxes and ocean heat uptake were sensitive to the vertical resolution near the surface.

5.4. Lateral Viscosity

As discussed above, numerical mixing is closely linked to near grid-scale variability in the velocity field and therefore is expected to be strongly influenced by the lateral viscosity (Griffies et al., 2000; Ilicak et al., 2012). In ACCESS-OM2-01, if the lateral biharmonic viscosity coefficient is increased by increasing the Smagorinsky scaling coefficient from 2 to 7.9 (ACCESS-OM2-01-hvisc in Table 1), there is a 20%–30% reduction in numerical mixing across most temperatures (compare magenta solid and dotted lines in Figure 7i). This reduction is consistent with the results of Ilicak et al. (2012) who found that increasing the Smagorinsky coefficient from 2 to 4 in a 1/4° MOM5 spin-down simulation reduced the spurious numerical mixing by a factor of about 1/3. The reduction in numerical mixing is associated mainly with regions where eddy variability is high (not shown), where increasing viscosity reduces spatial variability in the horizontal velocity at small scales (but does not overly influence temperature variability, see spectral analysis in Section 5.5). The difference in numerical mixing between ACCESS-OM2-01 and ACCESS-OM2-01-hvisc are not compensated by changes in vertical mixing (compare magenta lines in Figure 7e). Instead, the surface temperature structure and surface heat fluxes are altered such that there is less surface heat gain at warmer temperatures and less heat loss at colder temperatures (compare magenta lines in Figure 7a).

5.5. Horizontal Resolution

Three different horizontal grid spacings have been considered in this study; 1° - where eddy affects outside the tropics are largely parameterized, 1/4° - an "eddy-permitting" resolution where mesoscale eddies outside the tropics are marginally resolved and 1/10° - an "eddy-active" simulation where mesoscale eddies are captured away from the high-latitudes and shallow continental shelves (Hallberg, 2013). In general, comparisons across the model suite shown in Figure 7i and 7j, or quantified by $\mathcal{I}_{\text{net}}$ in Table 1, suggest that numerical mixing is strongest at 1/4°, somewhat weaker at 1/10° and weakest at 1°. However, comparisons of numerical mixing across standard configurations at these three horizontal resolutions is complicated by differences in explicit mixing coefficients (these choices are often made, at least in part, for reasons to do with numerical mixing). Here we compare two sets of configurations: ACCESS-OM2-1-KDS50 with ACCESS-OM2-025-NG-kbv and ACCESS-OM2-01 with ACCESS-OM2-025-KDS75 and ACCESS-OM2-01-hvisc (Figure 15), that are as close as possible in terms of explicit mixing parameters. These comparisons aim to draw some broad conclusions about changes in numerical mixing with horizontal resolution.

ACCESS-OM2-1-KDS50 and ACCESS-OM2-025-NG-kbv share the same vertical grid and vertical mixing schemes, but differ with respect to neutral diffusion (in addition to the grid-scale dependent lateral viscosity). ACCESS-OM2-025-NG-kbv has a weaker, grid-scale dependent neutral diffusion coefficient with maximum 200 $\text{m}^2\,\text{s}^{-1}$ compared with the constant value of 600 $\text{m}^2\,\text{s}^{-1}$ in ACCESS-OM2-1-KDS50. Note, however, that the diathermal heat transport due to neutral diffusion in the two configurations is similar (Figure 7g and 7h) suggesting that the enhanced creation of isopycnal temperature variance at 1/4° compensates for the weaker diffusion coefficient to first order. ACCESS-OM2-1-KDS50 has stronger explicit (vertical plus neutral) mixing, and weaker numerical mixing, across most of the temperature range (compare blue and black dashed lines in Figure 15b and 15c). While a small portion of this difference may be due to the difference in neutral diffusion coefficients, the fact that the differences in numerical mixing are larger than the differences in explicit mixing at temperatures warmer than ~7°C suggests that much of the increase in numerical mixing arises because of the enhanced velocity variability at 1/4° due to its admission of eddy variability.

ACCESS-OM2-025-KDS75 and ACCESS-OM2-01 both share the same vertical grid and the same explicit mixing parameter choices - differing only in their horizontal grid spacing and horizontal viscosity (they both use the same grid-scale dependent Smagorinsky coefficient of $C = 2$). Both configurations show similar levels of explicit mixing, while ACCESS-OM2-025-KDS75 shows slightly enhanced numerical mixing at temperatures characterizing the eddy-rich WBCs and ACC between 3°C and 20° (compare magenta and black solid lines in Figure 15c). These differences account for the slightly larger total numerical mixing in ACCESS-OM2-025-KDS75, $\mathcal{I}_{\text{net}} = 16.3\text{PW}^\circ\text{C}$, compared to ACCESS-OM2-01, $\mathcal{I}_{\text{net}} = 14.7\text{PW}^\circ\text{C}$.

However, if the lateral viscosity coefficient is instead kept more consistent as the horizontal resolution is increased from 1/4° to 1/10°, rather than decreasing with the grid-scale, then the reduction in numerical mix-

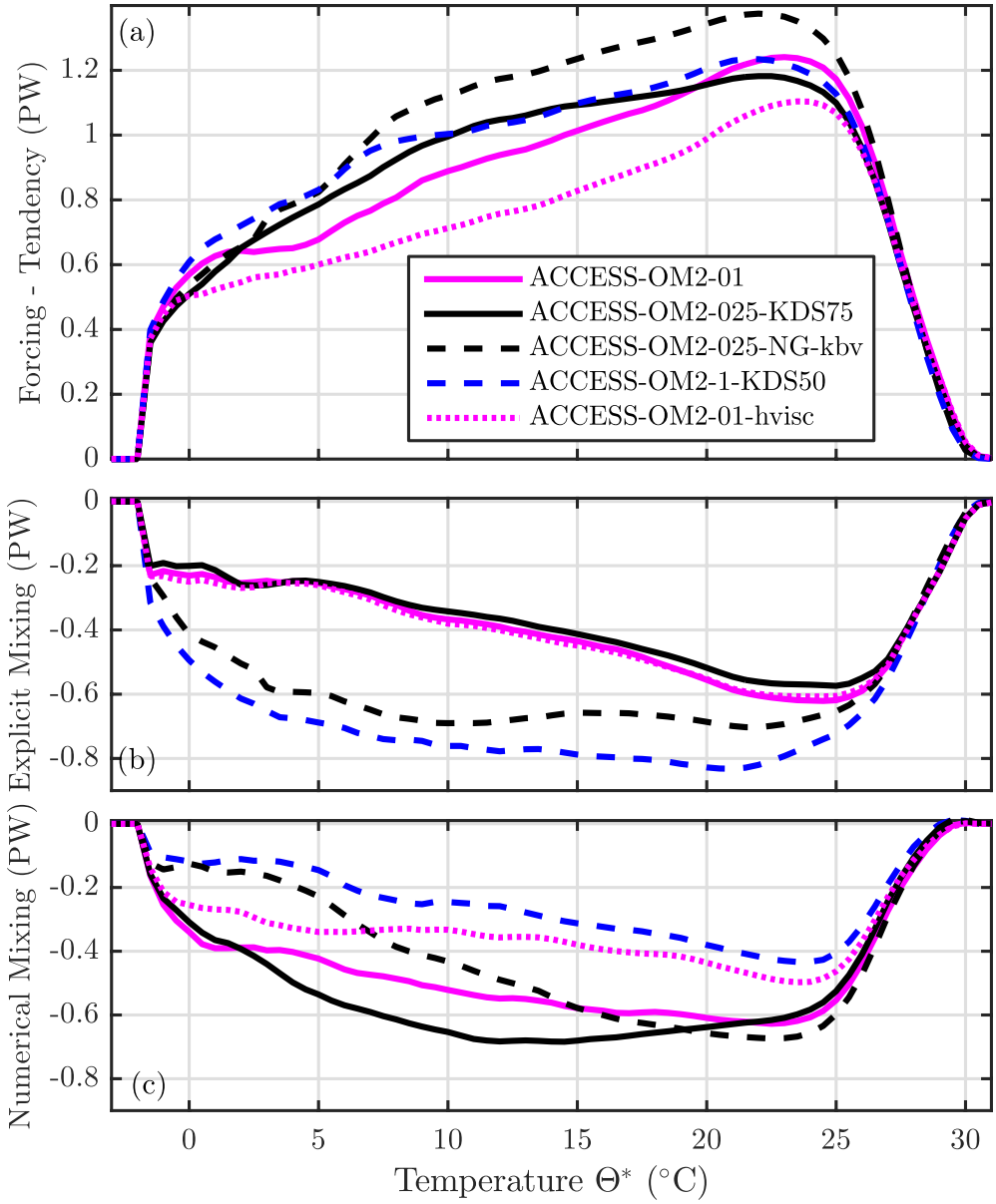

Figure 15. Global annually averaged diathermal heat budget terms (a) surface forcing minus tendency, $\mathcal{F}^g + \mathcal{P}_l^g - \partial\mathcal{H}_l^g/\partial t$, (b) explicitly parameterized mixing (neutral and vertical, $\mathcal{N}^g + \mathcal{M}^g$) and (c) numerical mixing, $\mathcal{I}^g$, in configurations chosen to compare across horizontal resolution. ACCESS-OM2-01-hvisc and ACCESS-OM2-025-KDS75 share the same vertical grid and explicit mixing parameters, and similar lateral viscosities. ACCESS-OM2-01 is the same as ACCESS-OM2-01-hvisc except that the lateral viscosity is reduced through the standard grid-scale dependent biharmonic scaling (Griffies & Hallberg, 2000). ACCESS-OM2-025-NG-kbv and ACCESS-OM2-1-KDS50 differ only in that the neutral diffusivity is larger in ACCESS-OM2-1-KDS50 and through the grid-scale dependent lateral viscosity. The vertical scale of every panel is the same to facilitate comparison.

ing is much more dramatic (compare ACCESS-OM2-01-hvisc and ACCESS-OM2-025-KDS75 in Figure 15c). This reduction reaches almost 50% at 12.5°C, while the total numerical mixing is reduced by almost 35% to $\mathcal{I}_{\text{net}} = 10.7$PW°C for ACCESS-OM2-01-hvisc compared to the 16.3PW°C in ACCESS-OM2-025-KDS75.

To quantify differences in velocity and temperature variability across scales and between the various horizontal resolution configurations, we plot horizontal kinetic energy and temperature spectra for a region in the Pacific sector of the Southern Ocean across our suite of simulations (Figure 16). ACCESS-OM2-1-KDS50 shows a steep drop off in kinetic energy at much larger scales than the other resolutions, reflecting

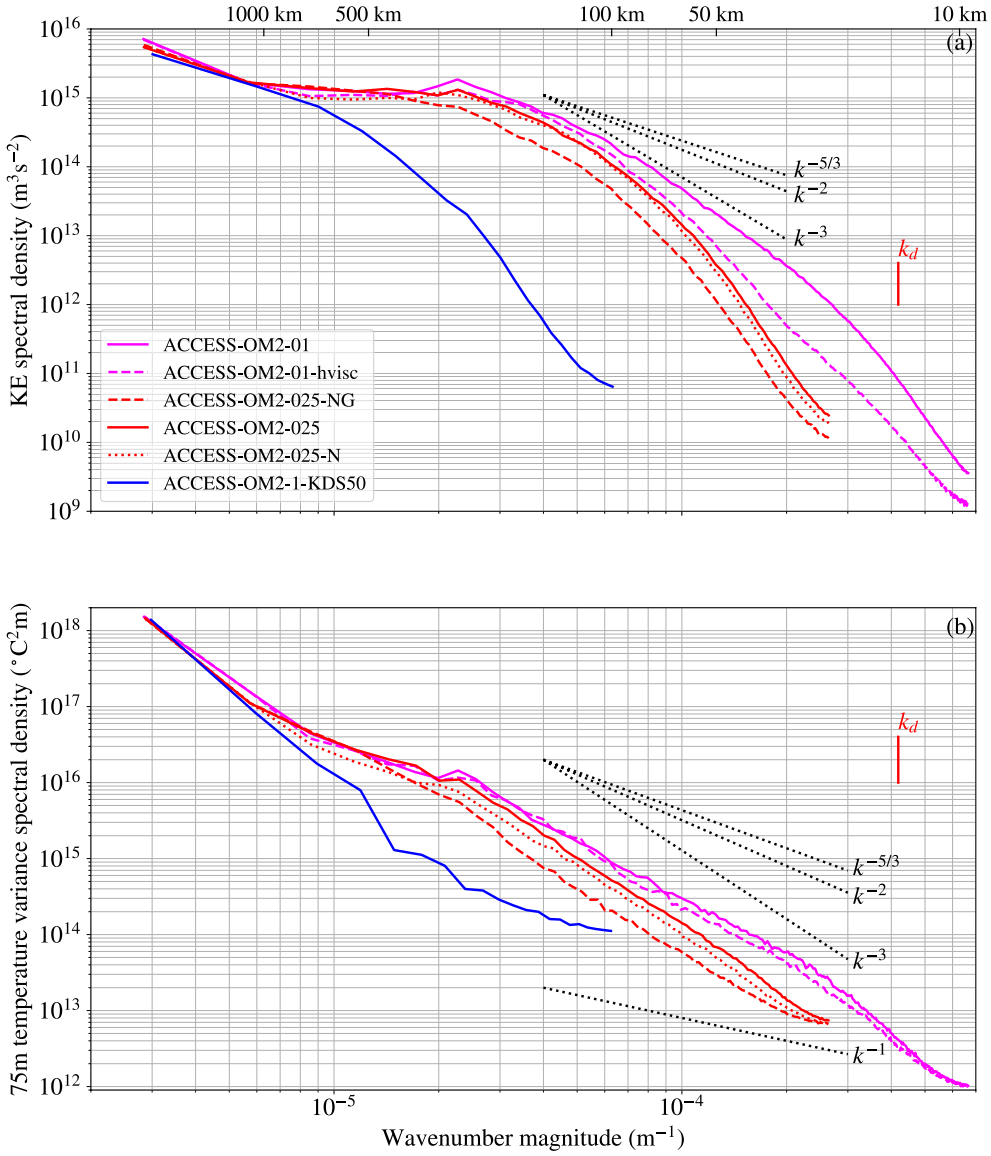

Figure 16. Horizontal wavenumber spectra of (a) surface kinetic energy and (b) temperature at 75 m depth from snapshots of the velocity and temperature fields at the end of each month in the Pacific sector of the Southern Ocean (65°S to 45°S, −180°E to −100°E, chosen as it is relatively isotropic and homogeneous) across a range of simulations. The spectra are computed following the methods of Durran et al. (2017) after interpolation onto a uniform Cartesian grid. Reference spectral slopes are shown with the black dotted lines. Corresponding wavelengths are shown at the top. The vertical red line marks the wavenumber k_d associated with the ∼15 km first-baroclinic deformation radius in this region (Chelton et al., 1998). Note that the spectra for ACCESS-OM2-025-KDS75 are similar to ACCESS-OM2-025 and spectra for ACCESS-OM2-025-NG-kbv are similar to ACCESS-OM2-025-NG (not shown).

the lack of an active eddy field (also see Kiss et al., 2020). In contrast, both the ACCESS-OM2-025 and ACCESS-OM2-01 configurations show a flatter spectrum at scales between ∼200 and ∼50 km. At larger scales in this range the spectral slope may be consistent with the $k^{-5/3}$ scaling expected for an inverse energy cascade from geostrophic turbulence theory (e.g., Charney, 1971). At smaller scales the slope drops off more steeply. However, in ACCESS-OM2-025 there is also a distinct flattening in the kinetic energy spectrum as the grid-scale is approached. This flattening may suggest that velocity variance is accumulating near the grid-scale in ACCESS-OM2-025, reflecting the marginal resolution of the eddy field and resulting in enhanced numerical mixing (these scales may be under-dissipated). Flattening of the spectra as the grid-scale is approached may also be because the dissipation for a biharmonic operator can become weaker as

the length scale decreases for scales near the grid-scale where the kinetic energy is low (e.g., see Section 4 of Soufflet et al., 2016). It should also be noted that the use of a second-order momentum advection scheme with fourth-order friction, as used in all these configurations, may lead to a range of scales where dispersion errors are not properly damped and provides another potential source of noise in the velocity fields. Alternative choices of momentum advection and friction schemes should be explored in future studies.

It is noteworthy that the ACCESS-OM2-025-NG configuration, where the GM scheme is active, has reduced kinetic energy across all scales finer than ~300 km due to a less active eddy-field, while ACCESS-OM2-025-N shows some slight reduction in kinetic energy at its smallest scales (compare red solid, dotted and dashed lines in Figure 16a). Comparison of spectra between ACCESS-OM2-01 and ACCESS-OM2-01-hvisc, where the Smagorinsky viscosity scaling factor has been increased from 2 to 7.9, highlights the important role of lateral viscosity (compare magenta solid and dashed lines in Figure 16a, also see Section 5.4). The kinetic energy in ACCESS-OM2-01-hvisc is significantly reduced even at scales well above the grid-scale, which may result from the reduction of up-scale energy transfer in the inverse cascade (alternatively, the biharmonic friction operator may have a direct impact on these scales that a higher-order operator would not).

The horizontal temperature variability spectra do not show the steepening evident in the kinetic energy spectra at smaller scales, except in ACCESS-OM2-01 at scales comparable to and below the first baroclinic deformation radius (Figure 16b). This lack of steepening may reflect the absence of any explicit horizontal diffusion operator (apart from the horizontal component of neutral diffusion when it is active). Instead, at scales approaching the grid-scale the horizontal temperature spectra tend to flatten. This flattening could reflect a transition to the viscous Batchelor regime (with an expected slope of k^{-1}, Batchelor, 1959), or that temperature variance is accumulating near the grid-scale. This near-grid-scale temperature variance may be caused by variable vertical velocities associated with the grid-scale horizontal velocity variability (e.g., Ilicak et al., 2012), resulting in numerical mixing. It is notable that the GM and neutral diffusion schemes have only a small impact on the horizontal temperature variability at scales near the grid-scale, although the presence of GM does reduce temperature variability at larger scales by reducing resolved eddy-stirring (compare red lines in Figure 16b).

Our comparison between ACCESS-OM2-025-KDS75 and ACCESS-OM2-01 suggests that numerical mixing is enhanced at 1/4° resolution, but only by about 10%. The marginal resolution of mesoscale eddies at 1/4° may lead to their velocity signatures at the grid-scale being noisy. While eddy formation is better resolved at 1/10°, and there appears to be less flattening in the kinetic energy spectrum as the grid-scale is approached, the cascade of temperature variance from large to small scales in eddying regimes always necessitates the dissipation of temperature variance near the grid scale (Roberts & Marshall, 1998). Thus the dependence of numerical mixing on horizontal resolution is not particularly strong. However, it is important to note that this comparison assumes that the viscosity is reduced as the grid-scale reduces (as is common in most GCMs). If instead the viscosity is kept more consistent as the resolution is increased then the permitted velocity variability is better resolved and thus the numerical mixing does decrease significantly (by almost 35% between ACCESS-OM2-025-KDS75 and ACCESS-OM2-01-hvisc).

6. Discussion and Summary

We have presented a method for quantifying the three-dimensional spatial and temporal structure of spurious numerical mixing within global ocean model simulations (Section 2). The method can be applied to any conservative tracer but is here applied to temperature. The method is based on constructing the budget for the "internal heat content" (Holmes et al., 2019a) of temperature layers within a given fluid column. The use of internal heat content removes much of the rapid variability in the heat content of temperature layers due to adiabatic and diabatic volume exchanges and therefore reduces the sensitivity of our results to noise compared with previous approaches based on diathermal or diapycnal volume transports (e.g., Lee et al., 2002; Megann, 2017; Urakawa & Hasumi, 2014). Combined with the use of precise online diagnostics, our method provides a detailed view of the spatial structure of numerical mixing within realistically forced global ocean model simulations (e.g., Figure 3).

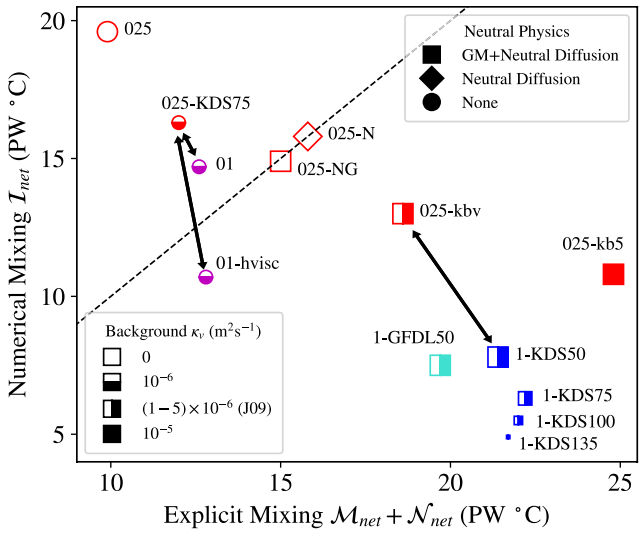

Figure 17. A summary of the total amount of numerical mixing (y-axis) and explicitly parameterized physical mixing (x-axis) in the various configurations considered in this article as quantified by the net heat variance dissipation rate diagnostic $\mathcal{I}_{net}$ (see Section 2.6) and its vertical mixing ($\mathcal{M}_{net}$) and neutral mixing ($\mathcal{N}_{net}$) counterparts. Blue, red and purple symbols indicate 1°, 1/4° and 1/10° configurations respectively. The symbol size is inversely proportional to the number of vertical levels. The different symbol types and symbol fills indicate the active neutral physics parameterizations and background vertical diffusivity, respectively, as indicated in the legends. Models lying above the dashed one-to-one line have more numerical mixing than explicit mixing and vice versa. The black arrows pair configurations with different horizontal resolutions which have as much as possible equivalent explicit mixing parameters (see Section 5.5 and Figure 15).

Applied to a suite of global MOM5-based ocean model simulations the method reveals that the contribution of numerical mixing to the global diathermal heat transport from warm to cold water is comparable to, and often larger than, that of the physically based parameterized vertical and neutral diffusion (Figures 2 and 7). These results are consistent with those of Megann (2017) who suggested that numerical mixing in NEMO was comparable or larger than physically based vertical mixing. Heat fluxes due to numerical mixing are largest in the eddying WBCs and ACC, the continental shelves and slopes and the tropical Pacific and Atlantic thermoclines (Figure 3) where small-scale horizontal velocity variability and both horizontal and vertical temperature variability is largest.

The sensitivity of numerical mixing to various model parameters is summarized in Figure 17 by comparing the net heat variance dissipation rate diagnostic $\mathcal{I}_{net}$ (corresponding to the area under the curve of the global diathermal heat transport due to numerical mixing, see Section 2.6), and its physical mixing counterpart, across the various configurations. Figure 17 illustrates the interplay between physical and numerical mixing, with larger physical mixing generally leading to smaller numerical mixing and vice versa. In particular, several of the 1/4° configurations and the default 1/10° configuration have more numerical mixing than physical mixing (they lie above the dashed one-to-one line in Figure 17).

Numerical mixing at colder temperatures in the eddying WBCs and ACC is sensitive to the presence of physical parameterizations for neutral diffusion and eddy-induced advection (GM) suggesting that a significant proportion of the numerical mixing is along-isopycnal (Section 5.1, compare squares, diamonds and circles in Figure 17). In contrast, numerical mixing in the tropics is more sensitive to the background vertical diffusion and vertical resolution (Sections 5.2 and 5.3, compare symbol size and fill in Figure 17). Combined with the fact that temperature variations dominate density variations in the tropics, the dependence of numerical mixing on the vertical diffusivity and resolution suggests that much of the numerical mixing in the tropics is diapycnal.

Numerical mixing is also sensitive to horizontal resolution, being smallest at 1° (where mesoscale eddies are largely absent) and largest at 1/4° (compare blue, red and purple symbols in Figure 17) for standard configurations. However, these standard configurations also differ with respect to parameterized explicit mixing coefficients. Comparing 1/4° and 1/10° configurations which share the same explicit tracer diffusion parameters and vertical resolution, differing only in their grid-scale dependent lateral biharmonic viscosity, suggests that numerical mixing is enhanced only by about 10% at the 1/4° eddy-permitting resolution (Figure 15, red and purple circles joined by short arrow in Figure 17). Our results thus suggest that while eddies are better resolved at 1/10°, the necessity of dissipating temperature variance at small scales due to its down-scale cascade in eddying regimes (Roberts & Marshall, 1998) means that numerical mixing is not strongly dependent on horizontal resolution once eddies are permitted. However, such a statement applies only when the horizontal viscosity is grid-scale dependent, as is the case in most GCMs. If the viscosity coefficient is instead kept consistent as resolution is increased from 1/4° to 1/10° then the numerical mixing is reduced by almost 35% (Figure 15, red and purple circles joined by a long arrow on the left of Figure 17). This result suggests that the common practice in global ocean modeling of reducing the viscosity as much as permitted by stability constraints, in order to maximize the range of "permitted" variability, comes at a cost and should be considered carefully. Instead, ensuring that permitted variability is well-resolved, if practical given computational constraints, provides a pathway to numerical convergence and physically instead of numerically controlled mixing. Of course, such choices must first be informed by a diagnostic analysis and quantification of numerical mixing such as provided by the method presented in this article.

While our current method is unable to quantitatively distinguish between the isopycnal and diapycnal components of numerical mixing it may be possible to generalize our approach by combining the heat and salt budget diagnostics (e.g., Hieronymus et al., 2014; Zika et al., 2015). However, nonlinearities in the equation of state may be more difficult to deal with and it is not clear that the properties of the internal heat content budget that we have taken advantage of here could be retained. Our results nevertheless indirectly suggest that the diapycnal component of numerical mixing is not negligible. While in this study we have taken the standard MOM5 numerical tracer advection scheme (MDPPM) as given, our results, along with previous studies (e.g., Ilicak et al., 2012; Megann, 2017) suggest that more attention should be paid to the choice of numerical tracer advection schemes, horizontal momentum advection and friction schemes as well as explicit mixing parameters in global ocean models.

It is encouraging that increasing the vertical resolution in the tropical ocean reduces numerical mixing there. Increases in the number of vertical levels, or simply changing the placement of the levels, provides an economical way to reduce numerical mixing. Similarly, increasing the horizontal viscosity also resulted in a clear reduction in numerical mixing. However, it is important to note that as numerical mixing is reduced explicit mixing parameters may need to be increased to compensate. The equatorial subsurface temperature biases shown in Figure 12 suggest that a minimum level of mixing in the upper ocean is required to reproduce the observed hydrographic structure.

While open questions remain, the method and diagnostics presented here provide a unique and clear geographic view of the impact of numerical discretization on the heat budget of global ocean models, with implications for model biases, heat transport (e.g., Holmes et al., 2019) heat uptake (Adcroft et al., 2019) and drift.

Appendix A: Numerical Methods

This appendix describes numerical details as to how the internal heat content budget is constructed (Section A1) and discusses some known issues with the method (Section A2) and their implications (Section A3).

A1. Numerical Construction of Temperature-Coordinate Budgets

The terms in the internal heat content budget (Equation 6) not involving the lateral fluxes $\mathcal{Q}$ and Ψ are calculated as described in HZE19 by binning the associated Eulerian heat budget diagnostic terms (for explicit (i.e., physical) mixing and surface forcing, e.g., $\mathcal{M}$, $\mathcal{N}$, $\mathcal{F}$ and $\mathcal{P}_l$ in Equation 6) online at every time step into temperature coordinates using the tracer cell center temperatures and a regular temperature grid with 0.5°C intervals. The internal heat content tendency term (LHS of Equation 6) is calculated using differences of snapshots of the temperature field and grid-cell thickness at the beginning and ending of each diagnostic accumulation period. However, unlike in HZE19, here we do not perform a global integral. The lateral terms, $\mathcal{Q}$ and Ψ, which vanish when integrated globally, are obtained by binning the Eulerian lateral heat and volume transports at the tracer-cell faces into temperature classes online at every time step, and then summing over all temperatures warmer than Θ^*. Note that the binning temperature used for $\mathcal{Q}$ and Ψ is the temperature linearly interpolated to the tracer-cell faces where the given flux is located. All terms in Equation 6 are located on temperature bin edges and no averaging in temperature coordinates is required.

In addition to advective transports associated with the resolved velocity, $\mathcal{Q}$ and Ψ should also include terms associated with the eddy parameterizations of Gent and McWilliams (1990) and Fox-Kemper et al. (2008). In the simulations considered in this article these parameterizations are formulated in the tracer equations using a skew-diffusive approach (Griffies, 1998). As described in Appendix B, when using the skew-diffusive lateral heat flux the eddy contribution to $\mathcal{Q}$ includes a term associated with the eddy-driven lateral volume flux that cancels with the corresponding term in the volume budget when formulating the internal heat content budget. Therefore, our analysis does not use the eddy-driven contribution to Ψ. While skew-diffusion itself should not drive any heat across isotherms, its numerical implementation may drive across-isotherm heat fluxes which are also captured in $\mathcal{I}$. However, we note that a global integral of the full three-dimensional convergence of the skew-diffusive heat fluxes in temperature coordinates suggests that the numerical mixing is dominated by that associated with the resolved velocity field.

A2. Known Issues

There are several known potential inaccuracies with the spatially resolved method.

A2.1. Temperature Binning of Flux Convergences

The temperature binning process assigns all of the heat flux convergence due to a given process to the cell mean temperature, which follows from a finite volume interpretation of the discrete tracer equation. In contrast, the numerical formulation of a given process may implicitly assume that there is some sub-grid-scale structure to the temperature field. Getzlaff et al. (2010) discuss some alternative binning methods.

A2.2. Temperature Binning of CLateral Transports

The binning of the lateral transports $\mathcal{Q}$ and Ψ is performed using the temperature linearly interpolated to the tracer-cell faces while the other terms use the tracer-cell center temperatures. This issue is related to the fundamental constraint on finite-volume advection schemes that the fluxes on cell faces must be related through some interpolation scheme to the non-co-located cell center tracer values. It is possible that improved results could be obtained using a more technically difficult up-winding system where the flux is binned according to the temperature of the tracer cell into which the flux is entering.

A2.3. Temperature Binning and Time Stepping

The binning of each Eulerian process tendency occurs once per time-step using the value of the temperature field before the time step. This choice is sensible but arbitrary. One could instead use the temperature field after it has been updated. Tests with a toy one-dimensional example (not shown) suggest that this error has a large impact on the binning of the native model total tendency and advection diagnostics (which are not used in the present method), but it does not strongly influence the binning of the other diabatic terms which vary more smoothly in time and space. One exception is the 1-degree model where the base configuration time step is a relatively large fraction of the diurnal cycle and thus the binning does not fully resolve the fast changes in near surface thermal stratification, short-wave penetration and convective mixing (see Section 5.3). It is also worth noting the different approach of Gibson et al. (2017) who perform a reference potential energy calculation between several sub-time step processes in MOM6, allowing the impacts of these different processes to be evaluated separately (in contrast, MOM5 does not use operator splitting - the tracer concentrations are updated only once per time step).

A2.4. The Sea Surface Height (SSH) Smoother

The lateral volume transport achieved by the Laplacian SSH smoothing operator (included to suppress a checkerboard null mode present in B-grid barotropic equations) is not included in the lateral volume flux convergence Ψ (although the impact of the SSH smoother is included in the heat flux convergence). The missing term leads to residuals in the vertically integrated volume budget of up to $\pm 10^{-7}$ m s^{-1} in regions where SSH gradients are strong such as the Gulf Stream and ACC (not shown).

A3. Comments on Noise, Uncertainties and Up-Gradient Fluxes

Physically based mixing, such as that from a Laplacian diffusion operator, smooths small scale structure. Consequently, a map of the diffusion time tendency exhibits enhanced power at the grid scale; i.e., it is "noisy". By extension, it is thus not surprising that any diagnosis of spurious mixing from truncation errors can also be prone to noise. The presence of noise makes it difficult to determine a confidence range on our results. The vertically integrated heat budget closes to much better than ± 1 W m^{-2}. Similarly, the neglect of the volume transport from the SSH smoother can be estimated using the vertically integrated volume budget residuals and approximate isotherm depths to have an impact of less than ± 1 W m^{-2} on $\mathcal{I}$. These errors are substantially lower than the 10–100 W m^{-2} values that we find for the diathermal heat transport due to numerical mixing across intermediate isotherms (Figure 3). However, it is not trivial to evaluate the impact of the other inaccuracies listed above.

Taking ACCESS-OM2-025 as an example, noise is apparent in $\mathcal{I}$ at small spatial scales near strong jets and frontal regions, where patches of small-scale large-magnitude positive and negative fluxes can appear (e.g., along the coastal extent of the Gulf Stream, Figure A1a). There are also some smaller magnitude up-gradient fluxes along the Equator (e.g., in the Western Pacific, Figure 3a) which are associated with the

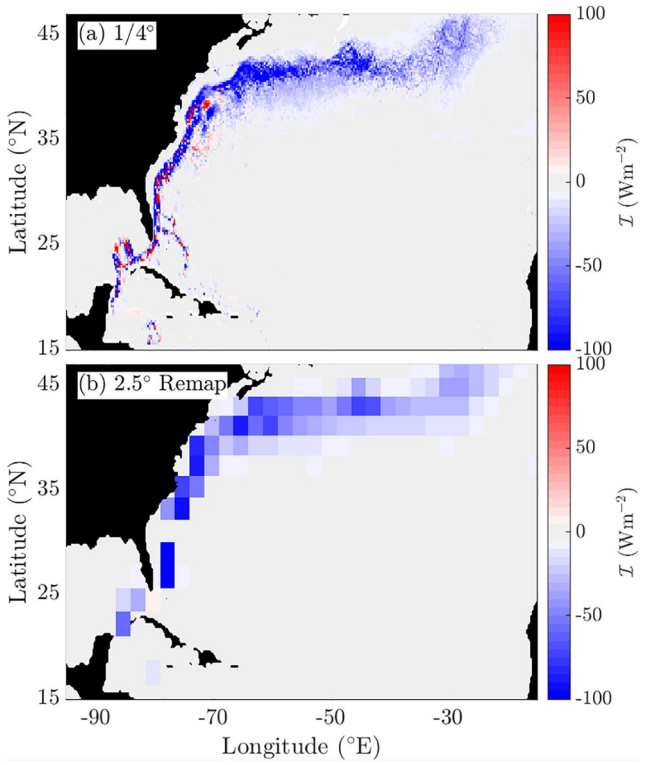

Figure A1. Heat flux through the 15°C isotherm due to numerical mixing in the North Atlantic from ACCESS-OM2-025 at (a) full resolution and (b) conservatively remapped to a coarse 2.5° grid.

coarse vertical grid spacing of the KDS50 grid in those regions (as discussed in Section 5.3). The Suresh and Huynh (1997) flux limiters on the MDPPM scheme should maintain monotonicity in the advected tracer distribution and prevent up-gradient fluxes. These up-gradient fluxes are not associated with the skew-diffusive submesoscale parameterization (established by turning this parameterization off, not shown) or GM or neutral diffusion (which are not active in ACCESS-OM2-025). Therefore, the presence of these small patches of up-gradient fluxes indicates that our method cannot accurately quantify numerical mixing at the grid-scale in these regions due to the approximations discussed above. However, when spatially averaged over larger regions including hundreds of grid points the fluxes are dominantly down-gradient (e.g., Figure A1b where the 1/4° map in Figure A1a has been conservatively remapped to a coarse 2.5° grid). Further temporal averaging also reduces this noise (not shown). We therefore restrict our analyses to discussing these larger scale patterns (although the spatially resolved metrics are presented at full resolution).

Appendix B: The Role of Skew-Diffusion in the Internal Heat Content Budget

The Gent and McWilliams (1990) and Fox-Kemper et al. (2008) parameterizations for eddy-driven transport are implemented in the model simulations using a skew-diffusive formulation as described in Griffies (1998). In this appendix we discuss the impact of skew-diffusion on the internal heat content budget of temperature layers within fluid columns and contrast it with an advective formulation. We consider a simple example described by Figure B1 where a temperature field $\Theta(y, z, t)$ defined in the meridional-vertical plane consists of isotherms (such as the Θ^* isotherm highlighted in orange) that slope upwards toward the north. For simplicity, we will assume that the ocean surface is a rigid lid with no surface volume fluxes, that salinity is constant (such that isopycnals and isotherms are synonymous) and that the only process that influences the temperature field is a parameterized eddy-driven circulation that will act to remove available potential energy by flattening isotherms. The eddy-driven circulation is characterized by a divergence-free eddy-induced velocity $\mathbf{v}^e$ related to an overturning streamfunction $\psi^e(y, z, t)$ by,

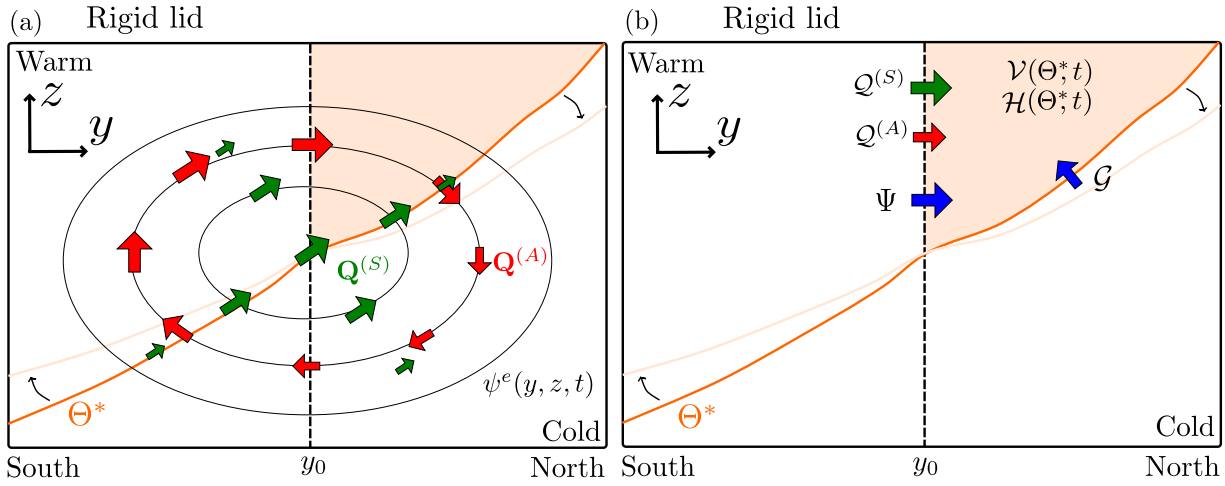

Figure B1. Schematic illustrating the impact of a parametrization for adiabatic eddy-driven tracer transport on the heat and volume budgets of temperature layers. In panel (a) an eddy streamfunction ψ^e (black contours) acts to flatten isotherms through the convergence of either an advective heat flux $\mathbf{Q}^{(A)}$ (red vectors) or a skew-diffusive heat flux $\mathbf{Q}^{(S)}$ (green vectors) whose divergences are equal. Panel (b) denotes various terms in the volume, $\mathcal{V}(\Theta^*,t)$, and heat, $\mathcal{H}(\Theta^*,t)$, budgets of the region bounded below by the Θ^* isotherm, above by the rigid lid and to the south by the fixed latitude y_0. These terms include the total advective, $\mathcal{Q}^{(A)}(\Theta^*,t)$, and skew-diffusive, $\mathcal{Q}^{(S)}(\Theta^*,t)$, heat transports across the y_0 latitude at temperatures above Θ^*, the volume transport, $\Psi(\Theta^*, t)$, across the y_0 latitude at temperatures above Θ^* as well as the across-isotherm volume transport $\mathcal{G}(\Theta^*,t)$ (equal to zero in this adiabatic example).

$$\mathbf{v}^e = -\psi^e_z \hat{\mathbf{j}} + \psi^e_y \hat{\mathbf{k}} \tag{B1}$$

where $\hat{\mathbf{j}}$ and $\hat{\mathbf{k}}$ are unit vectors in the meridional (y) and vertical (z) directions respectively.

The evolution of the temperature field is described by

$$\rho_0 C_p \frac{\partial \Theta}{\partial t} = -\nabla \cdot \mathbf{Q}, \tag{B2}$$

where $\mathbf{Q}$ is the heat flux. An *advective* formulation of the eddy-driven heat flux $\mathbf{Q}$ is given by

$$\mathbf{Q}^{(A)} = \rho_0 C_p \mathbf{v}^e \Theta = \rho_0 C_p \left(-\psi^e_z \Theta \hat{\mathbf{j}} + \psi^e_y \Theta \hat{\mathbf{k}}\right). \tag{B3}$$

In the situation described by Figure B1 a positive sign for ψ^e will result in a vector field $\mathbf{Q}^{(A)}$ (red vectors in Figure B1) that flattens isotherms. A *skew-diffusive* formulation for $\mathbf{Q}$ is instead captured by the heat flux

$$\mathbf{Q}^{(S)} = -\rho_0 C_p \mathbb{K}_S \cdot \nabla\Theta = \rho_0 C_p \left(\psi^e \Theta_z \hat{\mathbf{j}} - \psi^e \Theta_y \hat{\mathbf{k}}\right). \tag{B4}$$

In Equation B4, $\mathbb{K}_S$ is an anti-symmetric diffusivity tensor with zeros for the diagonal elements and $\pm\psi^e$ for the off-diagonal elements (e.g., see Griffies, 1998). The vector field $\mathbf{Q}^{(S)}$ (green vectors in Figure B1) is everywhere parallel to isotherms. It is easy to verify that the heat fluxes $\mathbf{Q}^{(S)}$ and $\mathbf{Q}^{(A)}$ differ only by a nondivergent vector field and therefore result in the same evolution of the temperature field.

We now consider the heat and volume budgets of the volume $\mathcal{V}(\Theta^*,t)$ bounded below by the Θ^* isotherm, above by the fixed rigid lid and to the south by the latitude y_0 (orange shaded region in Figure B1). The volume of this region evolves according to the motion of its boundaries

$$\frac{\partial \mathcal{V}}{\partial t} = \iint_{\partial \mathcal{V}} \mathbf{v}^b \cdot \hat{\mathbf{n}} \mathrm{d}\mathcal{S}, \tag{B5}$$

$$= \iint_{\Theta=\Theta^*} \mathbf{v}^b \cdot \hat{\mathbf{n}} \mathrm{d}\mathcal{S}, \tag{B6}$$

where $\mathbf{v}^b$ is the velocity of points on the boundary $\partial\mathcal{V}$ of the volume $\mathcal{V}$ over which the surface integral is performed (Groeskamp et al., 2019; Holmes et al., 2019b) and the normal vector $\hat{\mathbf{n}}$ is always directed out of the volume $\mathcal{V}$. In the second line we have used the fact that the rigid lid and the y_0 latitude boundary are fixed in space and thus the only moving boundary is the Θ^* isotherm. In this simple adiabatic example the across-isotherm volume transport $\mathcal{G}(\Theta^*,t)$ must vanish

$$\mathcal{G} = -\iint_{\Theta=\Theta^*}\left(\mathbf{v}^e - \mathbf{v}^b\right)\cdot\hat{\mathbf{n}}\,\mathrm{d}\mathcal{S} = 0 \tag{B7}$$

Using this in Equation B6, along with $\nabla\cdot\mathbf{v}^e = 0$, yields

$$\frac{\partial\mathcal{V}}{\partial t} = \Psi(\Theta^*,t), \tag{B8}$$

where $\Psi(\Theta^*, t)$ is the total volume transport across the y_0 latitude above the Θ^* isotherm (Figure B1).

The heat content of the region evolves according to

$$\frac{\partial\mathcal{H}}{\partial t} = \frac{\partial}{\partial t}\iiint_{\mathcal{V}}\rho_0 C_p\Theta\,\mathrm{d}V, \tag{B9}$$

$$= \rho_0 C_p\iiint_{\mathcal{V}}\frac{\partial\Theta}{\partial t}\mathrm{d}V + \rho_0 C_p\iint_{\partial\mathcal{V}}\Theta\mathbf{v}^b\cdot\hat{\mathbf{n}}\,\mathrm{d}\mathcal{S}, \tag{B10}$$

$$= -\iint_{\partial\mathcal{V}}\mathbf{Q}\cdot\hat{\mathbf{n}}\,\mathrm{d}\mathcal{S} + \rho_0 C_p\Theta^*\iint_{\Theta=\Theta^*}\mathbf{v}^b\cdot\hat{\mathbf{n}}\,\mathrm{d}\mathcal{S}, \tag{B11}$$

where in the second line we have used the Leibniz integral rule and in the third line we have used the divergence theorem to replace the temperature tendency with the surface integral of the heat flux $\mathbf{Q}$. For an advective formulation of the heat flux $\mathbf{Q}$

$$\frac{\partial\mathcal{H}}{\partial t} = -\iint_{y=y_0}\mathbf{Q}^{(A)}\cdot\hat{\mathbf{n}}\,\mathrm{d}\mathcal{S} - \iint_{\Theta=\Theta^*}\mathbf{Q}^{(A)}\cdot\hat{\mathbf{n}}\,\mathrm{d}\mathcal{S} + \rho_0 C_p\Theta^*\iint_{\Theta=\Theta^*}\mathbf{v}^b\cdot\hat{\mathbf{n}}\,\mathrm{d}\mathcal{S}, \tag{B12}$$

$$= \mathcal{Q}^{(A)} \qquad \left(\text{advective}\right) \tag{B13}$$

where in the second line we have realized that the last two terms cancel (as $\mathbf{Q}^{(A)} = \rho_0\, C_p\,\mathbf{v}^e\,\Theta^*$ on the Θ^* isotherm) and we have defined the total heat flux across the y_0 latitude as $\mathcal{Q}^{(A)}$ (Figure B1b). Combining Equation B13 with the volume budget (Equation B8) yields the internal heat content budget $\mathcal{V}$

$$\frac{\partial\mathcal{H}_I}{\partial t} = \frac{\partial\mathcal{H}}{\partial t} - \rho_0 C_p\,\Theta^*\frac{\partial\mathcal{V}}{\partial t} = \mathcal{Q}^{(A)} - \rho_0 C_p\,\Theta^*\Psi \qquad \left(\text{advective}\right) \tag{B14}$$

In contrast, for a skew-diffusive formulation of the heat flux $\mathbf{Q}$ the heat budget is

$$\frac{\partial\mathcal{H}}{\partial t} = -\iint_{y=y_0}\mathbf{Q}^{(S)}\cdot\hat{\mathbf{n}}\,\mathrm{d}\mathcal{S} - \iint_{\Theta=\Theta^*}\mathbf{Q}^{(S)}\cdot\hat{\mathbf{n}}\,\mathrm{d}\mathcal{S} + \rho_0 C_p\Theta^*\iint_{\Theta=\Theta^*}\mathbf{v}^b\cdot\hat{\mathbf{n}}\,\mathrm{d}\mathcal{S}, \tag{B15}$$

$$= \mathcal{Q}^{(S)} + \rho_0 C_p\Theta^*\Psi \qquad \left(\text{skew}\quad\text{diffusive}\right) \tag{B16}$$

where in the second line we have used the fact that $\mathbf{Q}^{(S)}$ is parallel to isotherms to eliminate the second term, used Equations B6 and B8 for the last term and defined the skew-diffusive heat transport across the y_0 latitude as $\mathcal{Q}^{(S)}$ (Figure B1b). The internal heat content budget is then

$$\frac{\partial\mathcal{H}_I}{\partial t} = \mathcal{Q}^{(S)} \qquad \left(\text{skew - diffusive}\right) \tag{B17}$$

Equation B17 shows that the eddy-driven volume flux Ψ across the y_0 latitude does not appear in the internal heat content budget when using a skew-diffusive formulation in contrast to an advective formulation (Equation B14). Of course, the effect on the internal heat content budget of the two formulations is still equivalent, because the skew-diffusive heat flux across the y_0 latitude $\mathcal{Q}^{(S)}$ (which is the diagnostic that we use to include the effects of skew-diffusion in the internal heat content budget) differs from the advective heat flux across the y_0 latitude $\mathcal{Q}^{(A)}$ exactly by the factor $\rho_0\, C_p\, \Theta^*\, \Psi$.

Data Availability Statement

The data required to reproduce the results in this article are published online (Zenodo, https://doi.org/10.5281/zenodo.4798380).

Acknowledgments
The authors thank Gurvan Madec, Mehmet Ilicak, Graeme MacGilchrist, Brandon Reichl and an anonymous reviewer for valuable comments on the manuscript and discussion. The authors thank K. Stewart for assistance with setting up the ACCESS-OM2-1 configurations. The authors thank the Consortium for Ocean and Sea-Ice Modelling in Australia (COSIMA) community for their valuable contributions to ACCESS-OM2 development. Modeling and analysis were undertaken using facilities at the National Computational Infrastructure (NCI), which is supported by the Australian Government. The authors are supported by the Australian Research Council (ARC)'s Centre of Excellence for Climate Extremes. J. Zika acknowledges support from ARC award DP190101173.

References

Adcroft, A., Anderson, W., Balaji, V., Blanton, C., Bushuk, M., Dufour, C. O., et al. (2019). The GFDL Global Ocean and Sea Ice Model OM4.0: Model description and simulation features. *Journal of Advances in Modeling Earth Systems*, *11*(10), 3167–3211. https://doi.org/10.1029/2019MS001726

Batchelor, G. K. (1959). Small-scale variation of convected quantities like temperature in turbulent fluid Part 1. General discussion and the case of small conductivity. *Journal of Fluid Mechanics*, *5*(1), 113–133. https://doi.org/10.1017/S002211205900009X

Bryan, K., Manabe, S., & Pacanowski, R. C. (1975). A global ocean-atmosphere climate model. Part II. The oceanic circulation. *Journal of Physical Oceanography*, *5*(1), 30–46. https://doi.org/10.1175/1520-0485(1975)005<0030:AGOACM>2.0.CO;2

Burchard, H., & Rennau, H. (2008). Comparative quantification of physically and numerically induced mixing in ocean models. *Ocean Modelling*, *20*(3), 293–311. https://doi.org/10.1016/j.ocemod.2007.10.003

Charney, J. G. (1971). Geostrophic turbulence. *Journal of the Atmospheric Sciences*, *28*(6), 1087–1095. https://doi.org/10.1175/1520-0469(1971)028<1087:gt>2.0.co;2

Chelton, D. B., deSzoeke, R. A., Schlax, M. G., El Naggar, K., & Siwertz, N. (1998). Geographical variability of the first baroclinic Rossby radius of deformation. *Journal of Physical Oceanography*, *28*(3), 433–460. https://doi.org/10.1175/1520-0485(1998)028<0433:GVOTFB>2.0.CO;2

Colella, P., & Woodward, P. R. (1984). The piecewise parabolic method (ppm) for gas-dynamical simulations. *Journal of Computational Physics*, *54*(1), 174–201. https://doi.org/10.1016/0021-9991(84)90143-8

Delworth, T. L., Rosati, A., Anderson, W., Adcroft, A. J., Balaji, V., Benson, R., et al. (2012). Simulated climate and climate change in the GFDL CM2.5 high-resolution coupled climate model. *Journal of Climate*, *25*(8), 2755–2781. https://doi.org/10.1175/JCLI-D-11-00316.1

Durran, D., Weyn, J. A., & Menchaca, M. Q. (2017). Practical considerations for computing dimensional spectra from gridded data. *Monthly Weather Review*, *145*(9), 3901–3910. https://doi.org/10.1175/MWR-D-17-0056.1

Fox-Kemper, B., Adcroft, A., Boning, C. W., Chassignet, E. P., Curchitser, E., Danabasoglu, G., et al. (2019). Challenges and prospects in ocean circulation models. *Frontiers in Marine Science*, *6*, 65. https://doi.org/10.3389/fmars.2019.00065

Fox-Kemper, B., Ferrari, R., & Hallberg, R. (2008). Parameterization of mixed layer eddies. Part I: Theory and diagnosis. *Journal of Physical Oceanography*, *38*(6), 1145–1165. https://doi.org/10.1175/2007JPO3792.1

Gent, P. R., & McWilliams, J. C. (1990). Isopycnal mixing in ocean circulation models. *Journal of Physical Oceanography*, *20*(1), 150–155. https://doi.org/10.1175/1520-0485(1990)020<0150:IMIOCM>2.0.CO;2

Gent, P. R., Willebrand, J., McDougall, T. J., & McWilliams, J. C. (1995). Parameterizing eddy-induced tracer transports in ocean circulation models. *Journal of Physical Oceanography*, *25*(4), 463–474. https://doi.org/10.1175/1520-0485(1995)025<0463:PEITTI>2.0.CO;2

Getzlaff, J., Nurser, G., & Oschlies, A. (2010). Diagnostics of diapycnal diffusivity in z-level ocean models part I: 1-Dimensional case studies. *Ocean Modelling*, *35*(3), 173–186. https://doi.org/10.1016/j.ocemod.2010.07.004

Gibson, A. H., Hogg, A. M., Kiss, A. E., Shakespeare, C. J., & Adcroft, A. (2017). Attribution of horizontal and vertical contributions to spurious mixing in an Arbitrary Lagrangian-Eulerian ocean model. *Ocean Modelling*, *119*, 45–56. https://doi.org/10.1016/j.ocemod.2017.09.008

Griffies, S., Adcroft, A., Banks, H., Böning, C., Chassignet, E., & Danabasoglu, G. (2009). Problems and prospects in large-scale ocean circulation models. *Proceedings of OceanObs*, *9*, 410–431.

Griffies, S. M. (1998). The Gent-McWilliams skew flux. *Journal of Physical Oceanography*, *28*(5), 831–841. https://doi.org/10.1175/1520-0485(1998)028<0831:TGMSF>2.0.CO;2

Griffies, S. M. (2004). *Fundamentals of ocean climate models*. Princeton. Princeton University Press.

Griffies, S. M. (2012). *Elements of the modular ocean model (MOM)*. GFDL Ocean Group Tech. Rep, 620.

Griffies, S. M., Gnanadesikan, A., Dixon, K. W., Dunne, J. P., Gerdes, R., Harrison, M. J., et al. (2005). Formulation of an ocean model for global climate simulations. *Ocean Science*, *1*(1), 45–79. https://doi.org/10.5194/os-1-45-2005

Griffies, S. M., Gnanadesikan, A., Pacanowski, R. C., Larichev, V., Dukowicz, J. K., & Smith, R. D. (1998). Isoneutral diffusion in a z-coordinate ocean model. *Journal of Physical Oceanography*, *28*, 805–830. https://doi.org/10.1175/1520-0485(1998)028<0805:IDIAZC>2.0.CO;2

Griffies, S. M., & Hallberg, R. W. (2000). Biharmonic friction with a smagorinsky-like viscosity for use in large-scale eddy-permitting ocean models. *Monthly Weather Review*, *128*(8), 2935–2946. https://doi.org/10.1175/1520-0493(2000)128<2935:BFWASL>2.0.CO;2

Griffies, S. M., & Treguier, A. M. (2013). Chapter 20 - Ocean circulation models and modeling. In G. Siedler, S. M. Griffies, J. Gould, & J. A. Church (Eds.), *Ocean circulation and climate* (pp. 521–551). Academic Press. https://doi.org/10.1016/B978-0-12-391851-2.00020-9

Griffies, S. M., Winton, M., Anderson, W. G., Benson, R., Delworth, T. L., Dufour, C. O., et al. (2015). Impacts on ocean heat from transient mesoscale eddies in a hierarchy of climate models. *Journal of Climate*, *28*(3), 952–977. https://doi.org/10.1175/JCLI-D-14-00353.1

Griffies, S., Pacanowski, R., & Hallberg, R. (2000). Spurious diapycnal mixing associated with advection in a z-coordinate ocean model. *Monthly Weather Review*, *128*(3), 538–564. https://doi.org/10.1175/1520-0493(2000)128<0538:SDMAWA>2.0.CO;2

Groeskamp, S., Griffies, S. M., Iudicone, D., Marsh, R., Nurser, A. G., & Zika, J. D. (2019). The water mass transformation framework for ocean physics and biogeochemistry. *Annual Review of Marine Science*, *11*(1), 271–305. https://doi.org/10.1146/annurev-marine-010318-095421

Hallberg, R. (2013). Using a resolution function to regulate parameterizations of oceanic mesoscale eddy effects. *Ocean Modelling*, *72*, 92–103. https://doi.org/10.1016/j.ocemod.2013.08.007

Hecht, M. W. (2010). Cautionary tales of persistent accumulation of numerical error: Dispersive centered advection. *Ocean Modelling*, *35*(3), 270–276. https://doi.org/10.1016/j.ocemod.2010.07.005

Hieronymus, M., Nilsson, J., & Nycander, J. (2014). Water mass transformation in salinity-temperature space. *Journal of Physical Oceanography*, *44*(9), 2547–2568. https://doi.org/10.1175/JPO-D-13-0257.1

Hill, C., Ferreira, D., Campin, J.-M., Marshall, J., Abernathey, R., & Barrier, N. (2012). Controlling spurious diapycnal mixing in eddy-resolving height-coordinate ocean models–insights from virtual deliberate tracer release experiments. *Ocean Modelling*, *45*, 14–26. https://doi.org/10.1016/j.ocemod.2011.12.001

Holmes, R. M., Zika, J. D., & England, M. H. (2019a). Diathermal heat transport in a global ocean model. *Journal of Physical Oceanography*, *49*(1), 141–161. https://doi.org/10.1175/JPO-D-18-0098.1

Holmes, R. M., Zika, J. D., & England, M. H. (2019b). Reply to 'Comments on "Diathermal heat transport in a global ocean model"'. *Journal of Physical Oceanography*, *49*(8), 2195–2197. https://doi.org/10.1175/JPO-D-19-0139.1

Holmes, R. M., Zika, J. D., Ferrari, R., Thompson, A. F., Newsom, E. R., & England, M. H. (2019). Atlantic Ocean heat transport enabled by indo-pacific heat uptake and mixing. *Geophysical Research Letters*, *46*, 13939–13949. https://doi.org/10.1029/2019GL085160

Hunke, E. C., Lipscomb, W. H., Turner, A. K., Jeffery, N., & Elliott, S. (2015). *CICE: The Los Alamos Sea Ice Model Documentation and Software User's Manual Version 5.1. Tech. Rep. LA-CC-06-012*. Los Alamos National Laboratory. Retrieved from http://oceans11.lanl.gov/trac/CICE/attachment/wiki/WikiStart/cicedoc.pdf?format=raw

Ilicak, M. (2016). Quantifying spatial distribution of spurious mixing in ocean models. *Ocean Modelling*, *108*, 30–38. https://doi.org/10.1016/j.ocemod.2016.11.002

Ilicak, M., Adcroft, A. J., Griffies, S. M., & Hallberg, R. W. (2012). Spurious dianeutral mixing and the role of momentum closure. *Ocean Modelling*, *45–46*, 37–58. https://doi.org/10.1016/j.ocemod.2011.10.003

Jochum, M. (2009). Impact of latitudinal variations in vertical diffusivity on climate simulations. *Journal of Geophysical Research*, *114*, C01010. https://doi.org/10.1029/2008JC005030

Kiss, A. E., Hogg, A. M., Hannah, N., Boeira Dias, F., Brassington, G. B., Chamberlain, M. A., et al. (2020). ACCESS-OM2 v1.0: A global ocean–sea ice model at three resolutions. *Geoscientific Model Development*, *13*(2), 401–442. https://doi.org/10.5194/gmd-13-401-2020

Klingbeil, K., Mohammadi-Aragh, M., Gräwe, U., & Burchard, H. (2014). Quantification of spurious dissipation and mixing–discrete variance decay in a finite-volume framework. *Ocean Modelling*, *81*, 49–64. https://doi.org/10.1016/j.ocemod.2014.06.001

Large, W. G., McWilliams, J. C., & Doney, S. C. (1994). Oceanic vertical mixing: A review and a model with a nonlocal boundary layer parameterization. *Review of Geophysics*, *32*(4), 363–403. https://doi.org/10.1029/94RG01872

Ledwell, J. R., St Laurent, L. C., Girton, J. B., & Toole, J. M. (2011). Diapycnal mixing in the Antarctic Circumpolar Current. *Journal of Physical Oceanography*, *41*(1), 241–246. https://doi.org/10.1175/2010JPO4557.1

Lee, M.-M., Coward, A. C., & Nurser, A. J. G. (2002). Spurious diapycnal mixing of the deep waters in an eddy-permitting global ocean model. *Journal of Physical Oceanography*, *32*(5), 1522–1535. https://doi.org/10.1175/1520-0485(2002)032<1522:SDMOTD>2.0.CO;2

Leonard, B. (1984). Third-order upwinding as a rational basis for computational fluid dynamics. Computational techniques and applications: CTAC-83 (pp. 106–120).

Lévy, M., Klein, P., Tréguier, A.-M., Iovino, D., Madec, G., Masson, S., & Takahashi, K. (2010). Modifications of gyre circulation by sub-mesoscale physics. *Ocean Modelling*, *34*(1), 1–15. https://doi.org/10.1016/j.ocemod.2010.04.001

MacGilchrist, G. A., Johnson, H. L., Marshall, D. P., Lique, C., Thomas, M., Jackson, L. C., & Wood, R. A. (2020). Locations and mechanisms of ocean ventilation in the high-latitude north Atlantic in an Eddy-Permitting Ocean Model. *Journal of Climate*, *33*(23), 10113–10131. https://doi.org/10.1175/JCLI-D-20-0191.1

Maqueda, M. M., & Holloway, G. (2006). Second-order moment advection scheme applied to Arctic Ocean simulation. *Ocean Modelling*, *14*(3), 197–221. https://doi.org/10.1016/j.ocemod.2006.05.003

Marchesiello, P., Debreu, L., & Couvelard, X. (2009). Spurious diapycnal mixing in terrain-following coordinate models: The problem and a solution. *Ocean Modelling*, *26*(3), 156–169. https://doi.org/10.1016/j.ocemod.2008.09.004

Margolin, L., Rider, W., & Grinstein, F. (2006). Modeling turbulent flow with implicit LES. *Journal of Turbulence*, *7*, 1–27. https://doi.org/10.1080/14685240500331595

Marshall, J., Jamous, D., & Nilsson, J. (1999). Reconciling thermodynamic and dynamic methods of computation of water-mass transformation rates. *Deep-Sea Research I*, *46*(4), 545–572. https://doi.org/10.1016/S0967-0637(98)00082-X

McDougall, T. J. (2003). Potential enthalpy: A conservative oceanic variable for evaluating heat content and heat fluxes. *Journal of Physical Oceanography*, *33*(5), 945–963. https://doi.org/10.1175/1520-0485(2003)033<0945:PEACOV>2.0.CO;2

McDougall, T. J., & Barker, P. M. (2011). Getting started with TEOS-10 and the Gibbs Seawater (GSW) oceanographic toolbox. *SCOR/IAPSO WG*, *127*, 1–28.

McDougall, T. J., Groeskamp, S., & Griffies, S. M. (2014). On geometrical aspects of interior ocean mixing. *Journal of Physical Oceanography*, *44*(8), 2164–2175. https://doi.org/10.1175/JPO-D-13-0270.1

Meehl, G., Gent, P. R., Arblaster, J., Otto-Bliesner, B., Brady, E., & Craig, A. (2001). Factors that affect the amplitude of El Niño in global coupled climate models. *Climate Dynamics*, *17*, 515–526. https://doi.org/10.1007/PL00007929

Megann, A. (2017). Estimating the numerical diapycnal mixing in an eddy-permitting ocean model. *Ocean Modelling*. https://doi.org/10.1016/j.ocemod.2017.11.001

Naughten, K. A., Galton-Fenzi, B. K., Meissner, K. J., England, M. H., Brassington, G. B., Colberg, F., et al. (2017). Spurious sea ice formation caused by oscillatory ocean tracer advection schemes. *Ocean Modelling*, *116*, 108–117. https://doi.org/10.1016/j.ocemod.2017.06.010

Redi, M. H. (1982). Oceanic isopycnal mixing by coordinate rotation. *Journal of Physical Oceanography*, *12*(10), 1154–1158. https://doi.org/10.1175/1520-0485(1982)012<1154:OIMBCR>2.0.CO;2

Richter, I. (2015). Climate model biases in the eastern tropical oceans: Causes, impacts and ways forward. *Wiley Interdisciplinary Reviews: Climate Change*, *6*(3), 345–358. https://doi.org/10.1002/wcc.338

Riemenschneider, U., & Legg, S. (2007). Regional simulations of the Faroe Bank Channel overflow in a level model. *Ocean Modelling*, *17*(2), 93–122. https://doi.org/10.1016/j.ocemod.2007.01.003

Roberts, M., & Marshall, D. (1998). Do we require adiabatic dissipation schemes in eddy-resolving ocean models? *Journal of Physical Oceanography*, *28*(10), 2050–2063. https://doi.org/10.1175/1520-0485(1998)028<2050:DWRADS>2.0.CO;2

Simmons, H. L., Jayne, S. R., Laurent, L. C. S., & Weaver, A. J. (2004). Tidally driven mixing in a numerical model of the ocean general circulation. *Ocean Modelling*, *6*(3), 245–263. https://doi.org/10.1016/S1463-5003(03)00011-8

Smith, K. S., & Ferrari, R. (2009). The production and dissipation of compensated thermohaline variance by mesoscale stirring. *Journal of Physical Oceanography*, *39*(10), 2477–2501. https://doi.org/10.1175/2009JPO4103.1

Solomon, H. (1971). On the representation of isentropic mixing in ocean circulation models. *Journal of Physical Oceanography*, *1*(3), 233–234. https://doi.org/10.1175/1520-0485(1971)001<0233:OTROIM>2.0.CO;2

Soufflet, Y., Marchesiello, P., Lemari, F., Jouanno, J., Capet, X., Debreu, L., & Benshila, R. (2016). On effective resolution in ocean models. *Ocean Modelling*, *98*, 36–50. https://doi.org/10.1016/j.ocemod.2015.12.004

Stewart, K., & Hogg, A. (2019). Southern ocean heat and momentum uptake are sensitive to the vertical resolution at the ocean surface. *Ocean Modelling*, *143*, 101456. https://doi.org/10.1016/j.ocemod.2019.101456

Stewart, K., Hogg, A., Griffies, S., Heerdegen, A., Ward, M., Spence, P., & England, M. (2017). Vertical resolution of baroclinic modes in global ocean models. *Ocean Modelling*, *113*, 50–65. https://doi.org/10.1016/j.ocemod.2017.03.012

Stewart, K., Kim, W., Urakawa, S., Hogg, A., Yeager, S., Tsujino, H., et al. (2019). Jra55-do-based repeat year forcing datasets for driving ocean-sea-ice models. *Ocean Modelling*, *147*, 101557. https://doi.org/10.1016/j.ocemod.2019.101557

Suresh, A., & Huynh, H. (1997). Accurate monotonicity-preserving schemes with Runge-Kutta time stepping. *Journal of Computational Physics*, *136*(1), 83–99. https://doi.org/10.1006/jcph.1997.5745

Tsujino, H., Urakawa, S., Nakano, H., Small, R. J., Kim, W. M., Yeager, S. G., et al. (2018). othersJRA-55 based surface dataset for driving ocean–sea-ice models (JRA55-do). *Ocean Modelling*, *130*, 79–139. https://doi.org/10.1016/j.ocemod.2018.07.002

Urakawa, L. S., & Hasumi, H. (2014). Effect of numerical diffusion on the water mass transformation in eddy-resolving models. *Ocean Modelling*, *74*, 22–35. https://doi.org/10.1016/j.ocemod.2013.11.003

Van Roekel, L., Adcroft, A. J., Danabasoglu, G., Griffies, S. M., Kauffman, B., Large, W., et al. (2018). The KPP boundary layer scheme for the ocean: Revisiting its formulation and benchmarking one-dimensional simulations relative to LES. *Journal of Advances in Modeling Earth Systems*, *10*(11), 2647–2685. https://doi.org/10.1029/2018MS001336

Walin, G. (1982). On the relation between sea-surface heat flow and thermal circulation in the ocean. *Tellus*, *34*(2), 187–195. https://doi.org/10.1111/j.2153-3490.1982.tb01806.x

Warner, S. J., Holmes, R., McHugh Hawkins, E. H., Hoecker-Martinez, M., Savage, A. C., & Moum, J. N. (2018). Buoyant gravity currents released from tropical instability waves. *Journal of Physical Oceanography*, *48*, 361–382. https://doi.org/10.1175/JPO-D-17-0144.1

Zika, J. D., Skliris, N., Nurser, A. G., Josey, S. A., Mudryk, L., Laliberté, F., & Marsh, R. (2015). Maintenance and broadening of the ocean's salinity distribution by the water cycle. *Journal of Climate*, *28*(24), 9550–9560. https://doi.org/10.1175/JCLI-D-15-0273.1